

SANDIA REPORT

SAND87-0880 • UC-70

Unlimited Release

Printed May 1987

Interim Results of Brine Transport Studies in the Waste Isolation Pilot Plant (WIPP)

E. J. Nowak, D. F. McTigue

Prepared by
Sandia National Laboratories
Albuquerque, New Mexico 87185 and Livermore, California 94550
for the United States Department of Energy
under Contract DE-AC04-76DP00789

*When printing a copy of any digitized SAND
Report, you are required to update the
markings to current standards.*

Issued by Sandia National Laboratories, operated for the United States Department of Energy by Sandia Corporation.

NOTICE: This report was prepared as an account of work sponsored by an agency of the United States Government. Neither the United States Government nor any agency thereof, nor any of their employees, nor any of their contractors, subcontractors, or their employees, makes any warranty, express or implied, or assumes any legal liability or responsibility for the accuracy, completeness, or usefulness of any information, apparatus, product, or process disclosed, or represents that its use would not infringe privately owned rights. Reference herein to any specific commercial product, process, or service by trade name, trademark, manufacturer, or otherwise, does not necessarily constitute or imply its endorsement, recommendation, or favoring by the United States Government, any agency thereof or any of their contractors or subcontractors. The views and opinions expressed herein do not necessarily state or reflect those of the United States Government, any agency thereof or any of their contractors or subcontractors.

Printed in the United States of America
Available from
National Technical Information Service
U.S. Department of Commerce
5285 Port Royal Road
Springfield, VA 22161

NTIS price codes
Printed copy: A05
Microfiche copy: A01

Distribution
Category UC-70

SAND87-0880
Unlimited Release
Printed May 1987

Interim Results of Brine Transport Studies in the Waste Isolation Pilot Plant (WIPP)

E. J. Nowak
Experimental Programs Division

D. F. McTigue
Fluid Mechanics and Heat Transfer Division I

Sandia National Laboratories
Albuquerque, NM 87185

Abstract

It is important to have quantitative predictions of brine movement in a radioactive waste repository for performance assessment and for seal design evaluations. Experiments to quantify brine transport to boreholes in multi-heater, full scale tests simulating high level waste repository environments have been under way in the bedded salt of the Waste Isolation Pilot Plant (WIPP) since April, 1985. Water vapor released to the test boreholes has been collected in flowing nitrogen and weighed periodically. Before heating, water was collected during several days from four test boreholes at rates in the range of 5 to 15 g/day. This result highlights the need for an isothermal model for brine movement in the WIPP host rock salt. After heating began, the water collection rates rose to a peak, decreased, and then remained nearly constant for several hundred days. Subsequently, trends to decreasing rates have been observed. Cumulative quantities of water were 4.3 kg at 441 days from each of two boreholes in Room A1 (with a 470 W heater in each borehole), and 36 to 38 kg at 600 days from each of the two boreholes in Room B (with a 1500 W heater in each borehole). After the early transients, approximately 8 g/day/borehole were collected in Room A1, and 50 to 80 g/day/borehole were collected in Room B. These are much larger brine inflow rates than were observed during heated brine migration tests in the domal salt of the Asse mine in the Federal Republic of Germany. Results from *in situ* brine transport tests in domal salt are not necessarily applicable to bedded salt.

A preliminary analysis of the results was begun with a highly idealized fluid flow model for porous media. Our water collection data for unheated boreholes agreed reasonably well with the brine inflows that were calculated with this model. Agreement was attained using permeability and porosity values that are generally consistent with measured WIPP host rock properties. It was also shown that the WIPP experiments are well within the transient stage of this model. However, the temperature dependence of viscosity, when used in this model, is inadequate to account for the large water collection rates in the heated boreholes. Further model development and additional experiments are needed to understand brine movement in the WIPP, with and without sources of heat. Parametric studies of time, scale, and salt composition are needed. Measurements of pore pressure at intervals within a few meters of WIPP excavations were shown by the model analyses to be important for testing mechanistic hypotheses concerning brine transport. WIPP hydrologic and disturbed zone characterization studies can also contribute to our mechanistic understanding of brine transport to WIPP excavations.

Contents

Abstract	ii
List of Figures	iv
List of Tables	iv
1 Introduction	1
2 Apparatus and Procedure	4
2.1 Overall system	4
2.2 Nitrogen flow and water measurement system	4
2.3 Procedure for moisture release measurements	5
3 Experimental Results	6
3.1 Nitrogen gas recovery and normalization of moisture release data	6
3.2 Room A1 — DHLW near-reference conditions	7
3.2.1 Measured cumulative water and collection rates	7
3.2.2 Response to change in nitrogen flow rate	7
3.2.3 Heater power	7
3.2.4 Borehole wall temperatures	7
3.2.5 Strain measurements	8
3.3 Room B — near-field overtest conditions	8
3.3.1 Measured cumulative water and collection rates	8
3.3.2 Heater power	9
3.3.3 Borehole wall temperature	9
3.3.4 Strain measurements	9
3.4 Discussion of experimental results	9
3.4.1 Comparison with previous models	9
3.4.2 Comparison with other experiments	10
3.4.3 General discussion of experimental results	11
3.4.4 Modeling needs	11
4 Preliminary Mechanistic Analyses of the Results	12
4.1 Assumptions and organization	12
4.2 Flow in a saturated, porous, linearly elastic medium	13
4.2.1 Introduction	13
4.2.2 Linear poroelasticity	13
4.2.3 Flow to a deep tunnel	15
4.2.4 Application to the moisture release experiments	18
4.2.5 Summary	20
4.3 Pore pressure profiles near WIPP rooms A1 and B	20

4.3.1	Introduction	20
4.3.2	Pressure profile	20
4.3.3	Application to rooms A1 and B	21
4.3.4	Summary	22
4.4	Effect of temperature-dependent viscosity	22
4.4.1	Introduction	22
4.4.2	Temperature-dependent viscosity	22
4.4.3	Numerical solution	24
4.4.4	Test problem	25
4.4.5	Summary	26
4.5	Long-term, steady-state, brine flow	26
4.5.1	Introduction	26
4.5.2	Steady flow to a line sink	27
4.5.3	Flow to a point sink	29
4.5.4	Summary and conclusions	29
5	Conclusions and Recommendations	31
6	References	33

List of Figures

1	Schematic diagram of the experimental system for each borehole.	36
2	Instrumentation and waste package emplacement WB1.	37
3	Instrumentation and waste package emplacement WB2.	38
4	Instrumentation and waste package emplacement WA1.	39
5	Instrumentation and waste package emplacement WA2.	40
6	Measured cumulative water <i>vs.</i> time, borehole A1041.	41
7	Measured cumulative water <i>vs.</i> time, borehole A1042.	42
8	Measured water inflow rate <i>vs.</i> time, borehole A1041.	43
9	Measured water inflow rate <i>vs.</i> time, borehole A1042.	44
10	Wall temperature, borehole A1041.	45
11	Wall temperature, borehole A1042.	46
12	Measured cumulative water <i>vs.</i> time, borehole B041.	47
13	Measured cumulative water <i>vs.</i> time, borehole B042.	48
14	Measured water inflow rate <i>vs.</i> time, borehole B041.	49
15	Measured water inflow rate <i>vs.</i> time, borehole B042.	50
16	Wall temperature, borehole B041.	51
17	Wall temperature, borehole B042.	52
18	Dimensionless flux <i>vs.</i> time for flow to a circular tunnel.	53
19	Dimensionless cumulative flux <i>vs.</i> time for flow to a circular tunnel.	54
20	Dimensionless pore pressure profiles due to flow to a tunnel.	55
21	Dimensionless radius and time at which pore pressure has relaxed to 50% and 75% of its initial value.	56
22	Comparison of exact analytical solution (squares) of (34)–(37) and numerical solution (circles) of (45)–(48).	57
23	Temperature profiles at $t = 1, 10,$ and 100 days.	58
24	Pressure profiles at $t = 1, 10,$ and 100 days.	58
25	Borehole wall temperature rise over 100 days (8.64×10^6 s).	59
26	Calculated brine flux for heated and unheated boreholes over 100 days .	59
27	Increase in fluid flux compared to increase in diffusivity.	60
28	Potential field for flow to a line sink (Eq. 58).	61
29	Streamlines corresponding to the potential field shown in Figure 28.	62
30	Comparison of transient (Eq. 30) and steady-state (Eq. 60) solutions for flux to a tunnel.	63

List of Tables

1	Model Parameters.	18
2	Calculated Flux, $t = 6$ mos. (Room A1).	19
3	Calculated Flux, $t = 10$ mos. (Room B).	19

4	Radius at which pore pressure has relaxed to 50%, 75%, and 90% of its initial value.	22
5	Model Parameters.	25
6	Calculated Borehole Temperature, Brine Flux, and Radius Where $p/p_0 = 0.9$	26

1 Introduction

The absence of circulating groundwater (brine) is a major advantage of rock salt as a host for radioactive waste isolation. This favorable characteristic of rock salt results in very slow mass transport through the undisturbed host rock.

Although bedded salt does not contain circulating groundwater, it is not completely dry. It contains approximately 0.1 to 1 wt% water as brine [1] that can, under certain conditions, move to boreholes, shafts, access drifts, and storage rooms where it can accumulate and introduce humidity. Brine can also migrate toward higher temperatures in temperature gradients such as those generated by heat-producing waste.

While the expected transport rates and total accumulations of this moisture are not likely to have an unacceptable impact on repository performance, it is important to have quantitative predictions of brine behavior for waste package and overall repository performance assessment and for the development of repository seal designs. Therefore, brine behavior is relevant to the evaluation of compliance with EPA standards for geologic disposal. Several aspects of brine behavior must be considered. Liquid brine may become entrapped in repository void spaces, promoting residual interconnected porosity that may adversely affect permeabilities within the repository. Brine entrapment may be significant in crushed salt reconsolidation. The permeabilities of reconsolidated salt components in shaft and panel seals are particularly important. Brine can also corrode waste containers and dissolve waste materials, creating a source pool of mobilized radionuclides. High relative humidity may increase pressurized gas generation by microbiological activity [2], causing added mechanical loads on seal structures and introducing additional considerations for repository failure scenarios. On the positive side, the desired reconsolidation of crushed salt seal components and backfills could be accelerated by a moderate rate of brine influx.

Mechanistic models of brine transport and release to backfilled and/or sealed repository excavations in bedded salt are needed for performance assessment. Gradients that can drive brine transport are created by mining activity and the presence of gas-generating and heat-producing wastes. The total pressure is atmospheric at the walls of an open excavation during the mining and operational phases. Far from the excavation, the pressure of brine in cavities and intergranular spaces may be near lithostatic, near hydrostatic, or at an intermediate value; the local pressures will depend on the extent of any hydraulic communication that exists within the body of salt. A pressure gradient will then exist in the salt between the wall and the far field. In a pore flow model, this gradient would be the pore pressure gradient. A water vapor pressure gradient (humidity gradient) that may drive water transport will also be set up by mine ventilation with unsaturated air. After the operational phase, these gradients may be eliminated or reversed by seal emplacements, closure, and gas generation. Heat flow from heat-producing waste will superimpose thermally induced mass transport driven by gradients of thermo-mechanical stress, vapor pressure and solubility (the driving force for brine inclusion migration). Heterogeneities in water content, mineral content, and pore structure that characterize bedded salt further complicate the system

of potentially important transport mechanisms that must be considered.

Previous efforts to quantify and model brine movement in salt have focused on thermally induced brine migration. These efforts resulted from concern about the potential effects of included brine on high-level waste (HLW) repository performance. Quantities of moisture as water vapor released from salt samples or collected in heated boreholes were measured and related to migrating brine inclusions as the source of the water [3-10]. Results from some of these studies were used to show that the migration of brine toward heat-producing waste containers is not likely to pose a significant problem for the isolation of radioactive waste in bedded salt [5]. However, these tests were not done *in situ* under the conditions of scale, geometry, and distributed thermal output that simulate a repository environment. Furthermore, it has since been found at the WIPP site that brines from fluid inclusions and brines collected from "weeps" and boreholes exhibit distinct chemical characteristics [11]. Thus, there is a strong indication that the source of the brine presently known to be transported into the facility is not fluid inclusions, and previous analyses of mechanisms of inclusion migration are not appropriate.

Intermediate scale brine migration tests in isolated heated boreholes have been under way in the Asse mine in the Federal Republic of Germany [12, 13]. These tests are located in a relatively pure, dry halite anticline that resulted from diapirism. Moisture that entered the test boreholes was swept out as water vapor in a gas stream, condensed, and measured. The operational, heated phase of these experiments has been completed. Relatively small quantities of water (approximately 0.1 kg in roughly 2 years) were collected during the heated phase of the Asse tests [13]. No water was collected before heating began. These results are consistent with models for brine migration in a relatively pure, dry, and homogeneous halite. They are not necessarily applicable to bedded salt. Experiments to quantify and model moisture release to heated boreholes in full scale, multi-borehole, multi-heater tests that simulate repository environments in bedded salt are now under way in the Waste Isolation Pilot Plant (WIPP) [14]. The WIPP project is a research and development facility intended to demonstrate the safe disposal of radioactive wastes in bedded salt. *In situ* tests in this facility address the technical issues surrounding repository development, waste package performance assessment, and waste handling demonstration [15, 16]. These *in situ* tests are located underground in the Salado formation of the Delaware Basin in southeastern New Mexico. The ongoing moisture release experiments have been a part of the near field effects/waste package full scale interactions tests [17] that simulate near-reference repository conditions for defense high-level waste (18 W/m² thermal areal loading with 470 W per canister) in underground test room A1 and near-field overtest conditions (1500 W per canister) in underground test room B. The procedure and apparatus are similar to those that have been used in some of the previous brine transport tests: moisture that is being released from the host rock salt to heated boreholes is removed continuously as water vapor in a nitrogen gas stream, collected, and measured. The test interval for these experiments is within the proposed WIPP waste storage level. Preliminary WIPP test results have highlighted the need for better models of thermally-induced brine move-

ment in the bedded salt of the Salado formation. Measured rates of moisture release in the heated WIPP tests have remained larger than the values that were predicted from models of brine inclusion migration, thermally-induced stress-gradient transport, and vapor phase transport in bedded salt [18]. During 321 days, 19.7 kg and 22.0 kg of water were collected from each of the room B (overtest thermal conditions) boreholes. At 320 days, 1.6 kg and 1.8 kg of water had been collected from each of the room A1 (near-reference thermal conditions) boreholes. Approximately 0.3 kg per borehole at 365 days was predicted for conditions similar to our overttest conditions from previous small scale tests and the models. There is a clear need to develop better models for thermally induced brine movement in the WIPP.

Preliminary WIPP results have also highlighted the need for an isothermal model of brine movement in the Salado, because significant quantities of moisture were also released to the test boreholes during several days before heating began [18]. Moisture release rates to WIPP test boreholes were in the range of 5 to 15 g/day per borehole before the borehole heaters were turned on [18]. A representative brine inflow rate of approximately $1.6 \text{ cm}^3/\text{day}/\text{m}^2$ at the depth of the WIPP facility was derived from these data for use in plugging and sealing design evaluations [19]. Another pertinent observation is apparent stratification of brine inflow as evidenced by horizontal bands of efflorescence in open boreholes. A mechanistic model for this inflow has not yet been fully developed and tested. Therefore, the proper dependence of brine inflow on depth, time, and size of excavation is currently unknown.

This is an interim report that presents additional results from the WIPP Moisture Release Experiment and a preliminary isothermal brine transport model that may assist in the interpretation of brine inflow measurements for unheated boreholes. After further development and testing, the model may be useful to predict brine inflow for unheated excavations. An analysis of data from unheated boreholes and an illustrative application of the model to unheated WIPP excavations will be emphasized in this report. The results and model will be compared with those that have been reported for other tests.

2 Apparatus and Procedure

2.1 Overall system

A schematic diagram of the experimental system is shown in Fig. 1. The physical locations of the boreholes (A1041, A1042, B041, and B042) for the moisture release experiment among the other boreholes for the WIPP near field effects/waste package interactions test is given elsewhere [17]. Moisture transport and release to these other boreholes may occur during the tests. Boreholes A1041 and A1042 in Room A1 are 46.6 m apart. Boreholes B041 and B042 in Room B are 28.5 m apart. Detailed drawings of these boreholes with simulated DHLW canisters and instrumentation are shown in Figs. 2–5. Electrical resistance heaters inside the canisters heat the lower 2.6 m sections of the vertical boreholes in the room floors. Heated borehole wall areas in the moisture collection zones are 9.9 m² for borehole B041 and 7.4 m² for boreholes B042, A1041, and A1042. Borehole wall temperatures are being measured with thermocouples. Strain at the borehole walls was determined with linear displacement gauges. Gauge and thermocouple placements are shown in Figs. 2–5. Displacement measurements are no longer reliable due to gauge deterioration at elevated temperatures and displacements that have exceeded the maximum measurable value. A discussion of the displacement gauge data appears elsewhere [18] and will not be treated in this report. Moisture that has been released to the borehole as water vapor is carried out in flowing nitrogen to a water collection and measurement system.

2.2 Nitrogen flow and water measurement system

Each borehole is equipped with a separate nitrogen flow and water vapor collection and measurement system. Dry bottled nitrogen passes through a flowmeter, a molecular sieve desiccant, and then an inlet tube to the bottom of each borehole. A vapor seal (packer) above each heater-canister prevents significant gas and vapor leakage. Nitrogen and water vapor leave the borehole through an outlet tube in the cover plate. The gas mixture from each borehole in Room B passes through a cold trap, a gas flow meter, and molecular sieve desiccant canisters that absorb more than 90% of the water vapor in the flowing gas. Only desiccants are used for Room A1 because of the smaller moisture release rates there. The mass of water collected in the desiccants and cold trap, normalized to 100% return of nitrogen from the borehole, is a measure of the moisture as water vapor that was released to the borehole during a measured time interval. Brine that has migrated to the borehole is assumed to be the source of the measured water.

The systems were originally designed to measure moisture release rates in the range of 0.0005 to 20 g/day using nitrogen flow rates from 10 to 1000 std. cc/min. The smallest measurable rate was fixed by the smallest controllable nitrogen flow rate and the equilibrium water vapor pressure specified for the desiccant (0.001 Torr for sodium aluminosilicate 4A molecular sieve). To achieve 95% collection efficiency, the minimum

allowable partial pressure of water was chosen to be 0.02 Torr. The maximum measurable rate was fixed by the largest nitrogen gas flow rate that could be obtained without appreciable leakage around the vapor seal due to excessive pressure buildup. Borehole pressures were established by the pressure drop in the long (as long as 100 m) nitrogen return tubes in the heated rooms. Input and return nitrogen flow data were used to calculate nitrogen flow material balances. Nitrogen flow material balances were used to normalize water collection data to 100% nitrogen recovery when the recovery was significantly less than 100%. Values for percent recovery will be discussed with the experimental results.

2.3 Procedure for moisture release measurements

Baseline data were taken before the borehole heaters were turned on. Zero time ($t = 0$) for each experiment was chosen to be the clock time for the first set of baseline data. Baseline data were taken over a 4-day interval for Room B and over a 7-day interval for Room A1. Then, heater power was initiated and increased to nominal values of 1500 W for Room B and 470 W for Room A1. Nominal heater power was reached within 2 minutes for all boreholes. The nitrogen flow rates were adjusted to keep the water collection rates safely within the design range as long as possible. Room B nitrogen flow rates were increased to the maximum allowable value after the water collection rates rose rapidly and finally reached the maximum measurable value. Subsequent replacement of the gas return tubing with a larger diameter raised the maximum allowable flow rate sufficiently to measure the moisture release rates in the Room B boreholes.

The desiccants were weighed and gas flowmeter readings were taken several times each workday initially and once each workday after the first few days. Nitrogen inlet and return flowmeter readings were taken just before the desiccants were weighed. The inlet and return flows were interrupted during the time (normally 10–20 minutes) that the desiccants were removed from the system for weighing. Temperature and displacement data were taken automatically at 15-minute intervals during the first several days and at 4-hour intervals thereafter.

3 Experimental Results

3.1 Nitrogen gas recovery and normalization of moisture release data

Moisture release data were normalized to 100% nitrogen gas recovery when nominally complete recovery was not indicated. Nitrogen carrier gas recovery was taken to be complete (nominally 100%) when the return flow rate reading was within 10% of the inlet flow rate reading. In that case, the quantity of collected water was assumed to be equal to the quantity of moisture that was released to a borehole. When the complete recovery criterion was not indicated, and the gas leaks could not be repaired within a few hours, the measured quantity of collected water was normalized to 100% gas recovery. It was assumed that the water vapor concentrations in the lost gas and the recovered gas were the same. To normalize data, the mass of collected water for a data interval was multiplied by the ratio of the gas flow rate during that interval to the average flow rate for a time interval of several days preceding the onset of incomplete recovery. The normalized mass value was assumed to be equal to the mass of moisture that was released to the borehole.

Results of diagnostic leak detection furnished a strong rationale for the normalization method that was employed. The only detectable gas leakage was around the vapor seals in the boreholes. The leak tests were carried out by temporarily replacing the nitrogen carrier gas with flowing helium. Then, the vapor seals, adjacent boreholes, nearby room surfaces, and flow system hardware were scanned for helium with a Gow Mac Model 21-110 Gas Leak Detector. Leaks small enough to be negligible for gas material balances were readily detected at the vapor seals in boreholes A1041 and B042. The larger leaks around the vapor seals in boreholes A1042 and B041 were orders of magnitude above the detection threshold. All moisture release results from boreholes A1041 and B042 met the criterion for complete gas recovery. The measured quantities of collected water were not normalized for those boreholes.

Leakage around the vapor seals into the air in the test rooms is consistent with the assumption that carrier gas was lost from the moisture collection zone where the water vapor content was equal to that of the returning gas. Furthermore, the lost water vapor would not be available for collection at some later time in the experiment. The observed leakage does not preclude the possibility that some carrier gas and water vapor enter the salt rock adjacent to the borehole. The observed leakage paths do, however, furnish a strong rationale for the data normalization method that was employed. Significant carrier gas losses began after 307 days ($t = 307$) for borehole A1042 and after 117 days ($t = 117$) for borehole B041. The ratio of inlet to return flow rates rose from 1.0 to 2.7 for borehole A1041 and to 2.0 for borehole B041.

3.2 Room A1 — DHLW near-reference conditions

3.2.1 Measured cumulative water and collection rates

Measured cumulative quantities of water from the boreholes in Room A1 are plotted versus time in Figs. 6 and 7. It was necessary to normalize water collection data for borehole A1042 (as described in Section 3.1.) to obtain measured cumulative quantities and rates, because nitrogen carrier gas recovery was significantly less than 100% after 307 days. Baseline (no heating) data were taken over a 7-day interval beginning at 0.0 days. After 441 days, 4.3 kg of water had been collected from each of boreholes A1041 and A1042. Details of the early time results have been reported elsewhere [18]; they will be summarized here. There were two transients characterized by large water collection rates, one immediately after initiating nitrogen flow and one approximately two days after heater turn-on. During the first 7.1 days before the heaters were turned on, 230 g of water were collected from borehole A1041, and 90 g of water were collected from borehole A1042. After brief transients, the water collection rates were nearly constant at 15 g/day and 7 g/day for A1041 and A1042, respectively during that initial period. Subsequently, the rates increased temporarily, then decreased gradually to approximately 8 g/day at 441 days, as shown in Figs. 8 and 9. The scattered data points are due to anomalies in the experimental operations such as gas flow-rate interruptions for diagnostic tests or repairs.

3.2.2 Response to change in nitrogen flow rate

At 103 days, the nitrogen flow rate for room A1 boreholes was reduced to 25% of the initial value. The water collection rate remained well within the measurable range. No change in water collection rates was detected at the new nitrogen flow rate, confirming that the measured rates were those of water release to the nitrogen and were not determined by the upper measurement limit for the apparatus.

3.2.3 Heater power

Heater power was nominally 470 W for the boreholes in Room A1. No power interruptions of more than a few seconds duration occurred. Average heater power was relatively constant at approximately 470 W. Early time heater power values have been published [18].

3.2.4 Borehole wall temperatures

Borehole wall temperatures at mid-heater height are plotted in Figs. 10 and 11 for the first 162 days. The wall temperatures increased to approximately 50 °C at 162 days. They increased gradually thereafter, reaching 55 °C in both boreholes at 441 days. The early time temperature histories have been published [18].

3.2.5 Strain measurements

Strain measurements are no longer reliable due to gauge limitations and deterioration at elevated temperatures. Early time strain data have been published [18]. No attempt will be made to interpret the strain data in this interim report.

3.3 Room B — near-field overtest conditions

3.3.1 Measured cumulative water and collection rates

Measured cumulative quantities of water for the boreholes in Room B are plotted versus time in Figs. 12 and 13. It was necessary to normalize water collection data for borehole B041 (as described in Section 3.1.) to obtain measured cumulative quantities, because nitrogen carrier gas recovery was significantly less than 100% after 117 days. Baseline (no heating) measurements were taken over a 4-day interval beginning at 0.0 days. After 600 days, 37.8 kg of water had been collected from borehole B041, and 35.7 kg had been collected from borehole B042. Water collection was characterized by a nearly constant small rate before heater turn-on and a rapidly increasing rate afterwards. During the first 4.2 days before the heaters were turned on, 22.4 g of water were collected from borehole B041 at an average rate of 5.4 g/day, and 19.3 g of water were collected from borehole B042 at an average rate of 4.6 g/day. After the heaters were turned on, the water collection rate increased to the practical upper limit on measurable rates (approximately 30 g/day) within approximately 2 days for both Room B boreholes. Water was no longer being collected and measured at the rate that it was being released to the borehole. Some water collected as condensate in the return gas lines, and some may have accumulated in the borehole. There is no reason to suspect that any significant quantity of water was lost from the water collection and measurement systems.

Daily quantities of collected water continued to be unreliable measures of water release rates until approximately 160 days. During that time, condensate was collected from the gas return lines, from uncooled liquid traps, and after 68 days from refrigerated liquid traps. After 105 days, larger diameter gas return tubing was put into service, and the upper limit on measurable water release rate was increased to 115 g/day. At approximately 160 days, there was no longer evidence of condensate in the return tubing, and water collection rates became less variable. A more detailed account of these early results has been published elsewhere [18].

After 160 days, the water collection rates remained relatively stable. For borehole B041, the normalized water collection rate rose to approximately 80 g/day at 200 days; then it decreased gradually to approximately 20 g/day at 600 days, as shown in Fig. 14. Because the nitrogen carrier gas recovery from borehole B041 continued to decrease, these results are to be regarded with less confidence than the results from B042. For borehole B042, as shown in Fig. 15, the water collection rate (calculated without normalizing) rose to approximately 65 g/day at 200 days; then it decreased gradually to approximately 50 g/day at 600 days.

3.3.2 Heater power

Heater power was nominally 1500 W for Room B boreholes. Several heater power interruptions and an interruption in power measurements occurred during the first 110 days of the Room B experiment. Transient changes in the water release rate that may have resulted from the heater power interruptions were not detected, because the upper limit on the measurement systems was exceeded during that time interval. After 120 days, the average heater power remained relatively constant at approximately 1500 W. Early time heater power data have been published elsewhere [18].

3.3.3 Borehole wall temperature

Borehole wall temperatures at mid-heater height are plotted in Figs. 16 and 17 for the first 321 days. The borehole walls reached temperatures between 115 °C and 125 °C at 321 days. Temperature fluctuations before 120 days were due primarily to heater power fluctuations. After 120 days, noise in the measurement and data acquisition system and power interruptions to surrounding heaters may account for the irregularities in the plotted data. Early time temperature data appear elsewhere [18]. The borehole wall temperatures increased gradually, reaching 120 °C in B041 and 130 °C in B042 at 600 days.

3.3.4 Strain measurements

Strain measurements are no longer reliable due to gauge limitations and deterioration at elevated temperatures. Early time strain data have been published [18]. No attempt will be made to interpret the strain data in this interim report.

3.4 Discussion of experimental results

3.4.1 Comparison with previous models

The measured quantities of water from heated boreholes in Rooms A1 and B are larger than the predictions from Shefelbein [5] for a hypothetical repository array of 2.16 kW canisters with 37 W/m² thermal load. Vapor phase transport (0.23 wt% water in salt), fluid inclusion motion (0.23 wt% water), and stress-gradient transport (0.3 wt% water) were evaluated by Shefelbein as predictive models. Stress-gradient transport yielded the largest cumulative water release: approximately 0.3 kg during the first year after emplacement. The boreholes in Room A1 (0.5 kW/canister) yielded 4.3 kg during the first 441 days, and the boreholes in Room B (1.5 kW/canister) yielded 37.8 kg and 35.7 kg during the first 600 days. While these quantities are relatively small compared with the initial repository void volume associated with a canister, they could be significant for canister corrosion. This experiment will be important in understanding the brine transport and inflow that occurs in a full-scale test as opposed to small scale experiments.

3.4.2 Comparison with other experiments

Other relatively large and long-term heated borehole tests have been under way in the Asse mine in the Federal Republic of Germany [12, 13]. These tests are located in a relatively pure, dry halite anticline that resulted from diapirism. Moisture was swept out of the boreholes as water vapor, condensed, and measured. The operational, heated phase of these experiments has been completed.

The quantities of measured water from the Asse tests were considerably smaller than the quantities from the ongoing WIPP tests. Approximately 0.1 kg was collected from each Asse test borehole during two years, with borehole wall temperatures reaching roughly 200 °C [13]. No collectible water was observed before heating began.

These results from the Asse tests are consistent with models for brine migration in a relatively pure, dry, and homogeneous halite. They are not necessarily applicable to bedded salt.

Differences in borehole wall area and water content of the salt are not sufficient to reconcile the differences between the WIPP and the Asse results. The WIPP/Asse ratio of test zone well areas is approximately 3, and the WIPP/Asse water content ratio is approximately 10. Area and water content scaling factors alone suggest that 30 times more water would be expected from the WIPP experiments than from the Asse experiments. According to that scaling factor, approximately 3 kg of water would have been collected from each Asse borehole during the 2 year duration of the Asse tests. These values are significantly smaller than the 36 kg to 38 kg that have been collected from Room B boreholes where the thermal conditions are most nearly equivalent to those at Asse.

Another difference between the WIPP and Asse results lies in the 5 to 15 g/day/borehole measured moisture release rate before heating in the WIPP tests. Also, visible brine pools were observed in nearby small, covered, WIPP boreholes before heating began. In the Asse tests, moisture release was unmeasurable before the heaters were turned on [13]. A non-thermal brine transport mechanism was operative in the WIPP tests; no such mechanism was detected in the Asse tests.

Differences between the characteristic properties of bedded and domal salt would appear to account for the large disagreement between the Asse and WIPP results. Compared with the bedded salt of the WIPP site, the Asse salt anticline that was formed by diapirism is likely to be characterized by tighter grain boundaries, more uniform grain size, and thinner, more generally discontinuous interbeds of clay and other minerals. Therefore, preferred flow paths for brine may be different and may present greater flow resistance than is the case at the WIPP test site.

Transport of brine to an unheated borehole was also observed in a previous small scale *in situ* experiment [5]. One of three boreholes was without heat for the first 124 days of the experiment while adjacent boreholes were heated to 145 °C (borehole wall temperature) in three steps. The water collection rate from the unheated borehole remained relatively constant and approximately the same as the rates from adjacent boreholes as they were heated to 90 °C. At 145 °C and higher, the rates from the heated

boreholes exceeded the rate from the unheated borehole.

3.4.3 General discussion of experimental results

The observation of larger water collection rates from Room B boreholes compared with Room A1 boreholes is consistent with previous observations [5]; moisture release rates are greater at higher heat input rates.

Water collection rates were independent of the partial pressure of water vapor in the boreholes. A four-fold decrease of nitrogen flow rate did not change the measured water collection rate. (See Reference [18] for more details.) Therefore, the partial pressure of water vapor in the boreholes must have increased by a factor of 4. Yet the release rate remained the same. This result is not consistent with water (or brine) transport mechanisms that depend on the the partial pressure of water vapor in the borehole. It follows that the evaporation rate of water at the borehole wall (potentially coupled with capillary flow of brine within the salt to the surface) is not a controlling mechanism for brine transport in these experiments.

There is evidence in the data for gradually decreasing measured release rates after a hundred or more days. For example, the water collection rate from borehole B042 rose to approximately 65 g/day at 200 days and then decreased to approximately 50 g/day at 600 days. The decrease may be due to geometric spreading of thee draining zone, or could be due a boundary effect if the brine flowing to these experiments is contained in a locally bounded domain of relatively permeable interconnected porosity.

3.4.4 Modeling needs

A mechanistic model is needed for preliminary analyses of these experimental results. We sought a model that would:

- match pre-heating water collection rates using values of flow properties (*e.g.*, permeability, porosity) that are in reasonable agreement with estimated host rock properties;
- predict relatively steady water collection rates for hundreds of days after the initial transients that follow heater turn-on;
- predict greater brine influx at higher heater power;
- include the possibility of locally bounded flow as well as globally connected flow;
- and suggest practical experiments to test the model and associated assumptions.

4 Preliminary Mechanistic Analyses of the Results

4.1 Assumptions and organization

A highly idealized fluid flow model for saturated porous media, widely used to describe groundwater flow in rocks and soils, shows promise for preliminary analyses of the experimental results. However, currently untested assumptions are inherent in this model. It is important to emphasize at the outset that there is currently no experimental evidence for our assumption of a totally saturated pore system after excavation and pore pressure between hydrostatic and lithostatic as a pre-excavation characteristic either of the Salado formation generally or of WIPP host rock salt. The value of the pre-excavation pore pressure that is actually used in the model (*i.e.*, hydrostatic or lithostatic, which are of the same order of magnitude) has little or no influence on the primary objective for the modeling exercise: to provide physical insight by revealing qualitative model behavior for comparison with the data from short-term tests.

Other untested assumptions are that there exists a relatively homogeneous body of interconnected porosity surrounding the excavations and that one can invoke the elastic behavior of the host rock salt matrix and the brine to characterize the transient pore pressure behavior. According to this model, most of the early time brine inflow (during the transient period following excavation) is due to decreasing brine storage in the host rock. It will be shown later that the WIPP moisture release experiments are occurring within the transient period of this model.

These assumptions were chosen to facilitate a relatively rapid preliminary evaluation of potential brine transport processes for data analyses and to provide physical insight for further model development. They were also useful to project best current estimates of brine influx values to tens of years for the design evaluation of WIPP shaft and panel seals. It is in longer-term predictions of total brine inflow, to hundreds of years and beyond, that assumptions concerning the extent of hydraulic communication in the host rock salt and the consequent pre-excavation pore pressure distribution become crucial. Accurate models that have been tested with *in situ* experiments are necessary in order to make meaningful long term brine inflow predictions.

The mechanistic analyses are subdivided into four subsections. Subsection 4.2 contains the development of the model for fluid flow consequent to the introduction of an excavation deep in a fluid-saturated, porous, linearly elastic medium. In Subsection 4.3, an estimate is made of the distance away from the tunnel walls to which the flow can be expected to reduce the fluid pressure significantly. The aim of this estimate is to provide guidance for field experiments designed to measure these pore pressures directly. In Subsection 4.4, the analysis of Subsection 4.2 is extended in order to assess the importance of the reduced fluid viscosity in the neighborhood of a heat source. Finally, in Subsection 4.5, the long-term, steady-state flow to a deep tunnel due to flow under hydrostatic pressure through rigid, porous rock is treated to provide justification for the simplified transient model that was used in the data analyses.

4.2 Flow in a saturated, porous, linearly elastic medium

4.2.1 Introduction

Any model for transient flow of fluid in a porous medium requires the stipulation of a mechanism of “storage,” *i.e.*, local changes of fluid mass per unit volume of the medium. In a rigid porous medium, the only available mechanism is compression, or local density change, of the fluid. In a deformable porous medium, storage can be accommodated by dilatation of the solid skeleton and local compression of the solid, as well. Dilatation of the porous solid is the principal mechanism of general interest in soil and rock mechanics, and is the cornerstone of classical “consolidation” theory. Admittedly, rock salt exhibits plastic as well as elastic properties. It is, however, plausible that the immediate, elastic response (compression) of the salt and brine and the subsequent relaxation of the pore pressure by flow to the excavation are the predominant mechanisms of brine storage and transport over short time scales. For a linearly elastic skeleton, Biot [21] generalized the consolidation theory, and Rice and Cleary [20] later recast it in terms with straightforward physical interpretations. This model is often referred to as the theory of “poroelasticity.” Its essential elements are summarized in the next section.

4.2.2 Linear poroelasticity

The linearized mass balance for the fluid constituent in a saturated porous medium can be written

$$\gamma_{f0} \frac{\partial \phi}{\partial t} + \phi_0 \frac{\partial \gamma_f}{\partial t} + \gamma_{f0} \nabla \cdot [\phi_0 (\mathbf{v}_f - \mathbf{v}_s)] + \gamma_{f0} \phi_0 \nabla \cdot \mathbf{v}_s = 0, \quad (1)$$

where γ_f is the local fluid density (fluid mass per unit volume of fluid), ϕ is the porosity, \mathbf{v}_f is the fluid velocity, \mathbf{v}_s is the solid velocity, and subscript zeros indicates constant reference values. Constitutive equations for the porosity change, fluid density, Darcy velocity, and strain are given by

$$\phi - \phi_0 = \left(\frac{1 - \phi_0}{K} - \frac{1}{K_s} \right) \left(\frac{1}{3} \text{tr} \mathbf{T} + p \right), \quad (2)$$

$$\gamma_f = \gamma_{f0} \left(1 + \frac{p}{K_f} \right), \quad (3)$$

$$\phi_0 (\mathbf{v}_f - \mathbf{v}_s) = - \frac{k}{\mu} \nabla p, \quad (4)$$

$$\mathbf{E} = \frac{1}{2G} \left[\mathbf{T} - \frac{\nu}{1+\nu} (\text{tr} \mathbf{T}) \mathbf{1} \right] + \frac{1}{3} \left(\frac{1}{K} - \frac{1}{K_s} \right) p \mathbf{1}, \quad (5)$$

where K is the “drained” bulk modulus characterizing the bulk stiffness of the skeleton at zero pore pressure, K_s is the bulk modulus of the solid constituent, \mathbf{T} is the total stress (or the “confining” stress in many geotechnical configurations), p is the pore

pressure, K_f is the bulk modulus of the fluid constituent, k is the permeability, μ is the fluid viscosity, \mathbf{E} is the solid strain, G is the elastic shear modulus for the skeleton, ν is the “drained” Poisson’s ratio, and $\mathbf{1}$ is the unit tensor. Also, for small deformation, the solid dilatation rate can be identified with the volumetric strain rate:

$$\nabla \cdot \mathbf{v}_s = \frac{\partial}{\partial t} (\text{tr} \mathbf{E}). \quad (6)$$

The governing equations are completed by a statement of strain compatibility, which, contracted twice, is given by

$$\nabla^2(\text{tr} \mathbf{E}) - \nabla \cdot (\nabla \cdot \mathbf{E}) = 0, \quad (7)$$

and the equilibrium equation for quasi-static deformation:

$$\nabla \cdot \mathbf{T} = 0. \quad (8)$$

After some manipulation, (1)–(7) can be combined to yield a diffusion equation of the form

$$\left(\frac{\partial}{\partial t} - c \nabla^2 \right) \left(\text{tr} \mathbf{T} + \frac{3}{B} p \right) = 0, \quad (9)$$

where

$$c = \frac{k}{\mu} \frac{2G(1-\nu)}{1-2\nu} \left[\frac{B^2(1+\nu_u)^2(1-2\nu)}{9(1-\nu_u)(\nu_u-\nu)} \right],$$

$$\frac{1}{B} = 1 + \phi_0 \frac{K}{K_f} \frac{1-K/K_s}{1-K/K_s},$$

$$\nu_u = \frac{3\nu + B(1-2\nu)(1-K/K_s)}{3-B(1-2\nu)(1-K/K_s)}.$$

The fluid diffusivity, c , is commonly called the “consolidation coefficient.” The parameter B is a measure of the fraction of an applied load that is born by the fluid under undrained conditions. This is apparent in the expression for the “change in fluid content” [21], or relative dilatation of the solid and fluid [22]:

$$\phi_0(\text{tr} \mathbf{E} - \text{tr} \mathbf{E}_f) = \left(\frac{1}{K} - \frac{1}{K_s} \right) \left(\frac{1}{3} \text{tr} \mathbf{T} + \frac{1}{B} p \right), \quad (10)$$

where $\text{tr} \mathbf{E}_f$ is the fluid dilatation. In an undrained loading, there is no displacement of fluid relative to the solid, so that $\phi_0(\text{tr} \mathbf{E} - \text{tr} \mathbf{E}_f) = 0$, and $p = -B \text{tr} \mathbf{T}/3$. For incompressible fluid ($K_f \rightarrow \infty$) and solid ($K_s \rightarrow \infty$) constituents, B is unity, and the term in brackets in the expression for the diffusivity is unity as well. In this case, the diffusivity reduces to its most common form as used in the soil mechanics literature:

$$c = \frac{k}{\mu} \frac{2G(1-\nu)}{1-2\nu}.$$

Neglect of the solid compressibility only ($K_s \rightarrow \infty$) yields

$$c = \frac{k}{\mu} \frac{2G(1-\nu)}{1-2\nu} \left[1 + \frac{3\phi_0(1-\nu)}{1+\nu} \frac{K}{K_f} \right]^{-1},$$

which is equivalent to the expression used by Bredehoeft [23] if one makes the identities $E_m = 3K(1-\nu)/(1+\nu)$ and $E_f = K_f$. The “undrained Poisson’s ratio,” ν_u , is also introduced for convenience.

4.2.3 Flow to a deep tunnel

Consider now a highly idealized model for the introduction of a mined drift into a deeply-buried region. The rock is assumed to be homogeneous and isotropic, and the undisturbed stress state is taken to be lithostatic, *i.e.*, isotropic, compressive, and equal in magnitude to the overburden load.¹ Thus, in a cylindrical polar coordinate system centered at depth d below the surface, the undisturbed stress \mathbf{T}_0 is given by

$$\mathbf{T}_0 = -\sigma_0 \left(1 - \frac{r}{d} \cos \theta \right) \mathbf{1}, \quad (11)$$

where $\sigma_0 = \gamma_t g d$, γ_t is the density of the overburden (rock plus pore fluid), g is the acceleration of gravity, r is the radial coordinate, and θ is the angle measured from the vertical. In the neighborhood of a circular tunnel of radius a , centered at $r = 0$,

$$\mathbf{T}_0 = -\sigma_0 \left[1 + O\left(\frac{a}{d}\right) \right] \mathbf{1}. \quad (12)$$

For a tunnel of radius $a = 3.5$ m at depth $d = 600$ m, considered in the present case, $a/d \sim O(10^{-2})$, and it is reasonable, within several tunnel radii, to make the approximation

$$\mathbf{T}_0 \simeq -\sigma_0 \mathbf{1}. \quad (13)$$

Because the far-field confining stress is assumed to be isotropic (13), the deformation around a circular tunnel must be axisymmetric. In plane strain, the strains are then given by

$$E_{rr} = \frac{\partial u_r}{\partial r}, \quad (14)$$

$$E_{\theta\theta} = \frac{u_r}{r}, \quad (15)$$

where u_r is the radial displacement. Substitution of (14) and (15) into (5) yields the stresses in terms of the displacement u_r , and pressure p . Substitution of these into the equilibrium equation (8) gives

$$\frac{\partial}{\partial r} \left[\frac{1}{r} \frac{\partial}{\partial r} (ru_r) \right] = \frac{3(\nu_u - \nu)}{2GB(1-\nu)(1+\nu_u)} \frac{\partial p}{\partial r}, \quad (16)$$

¹The latter assumption, of course, ignores the observation that the horizontal stresses in most crustal rocks are less than the vertical stress. Creep, however, tends to relax these principal stress differences.

which can be integrated to yield

$$u_r = \frac{3(\nu_u - \nu)}{2GB(1-\nu)(1+\nu_u)} \frac{1}{r} \int_a^r p(\xi, t) \xi d\xi + r c_1(t) + \frac{1}{r} c_2(t), \quad (17)$$

where $c_1(t)$ and $c_2(t)$ are arbitrary functions of time. If $\lim_{r \rightarrow \infty} u_r = 0$, one must take $c_1(t) = 0$. In this case, substitution of (17) into (14) and (15) and the resulting strains into (5) yields

$$\text{tr} \mathbf{T} = -\frac{6(\nu_u - \nu)}{B(1-\nu)(1+\nu_u)} p. \quad (18)$$

Thus, the mean stress is related directly to the pressure in this special case, and the diffusion equation (9) can be written in terms of the pressure alone; for one-dimensional, radial flow:

$$\frac{\partial p}{\partial t} - \frac{c}{r} \frac{\partial}{\partial r} \left(r \frac{\partial p}{\partial r} \right) = 0. \quad (19)$$

The plane strain solution for the stresses outside a circular tunnel of radius a , subject to equal principal stresses $-\sigma_0$ in the far-field, is well known:

$$T_{rr} = -\sigma_0 \left(1 - \frac{a^2}{r^2} \right), \quad (20)$$

$$T_{\theta\theta} = -\sigma_0 \left(1 + \frac{a^2}{r^2} \right), \quad (21)$$

$$T_{zz} = -2\nu_u \sigma_0. \quad (22)$$

The undrained Poisson's ratio appears because interest is focused here on the stress state immediately after introduction of the tunnel, prior to any effects due to pore fluid flow. Note that the assumption of plane strain is not compatible with the assumed isotropic stress state in the far field (13), *i.e.*, the axial stress, T_{zz} (22), does not have the correct far-field limit, $\lim_{r \rightarrow \infty} T_{zz} = -\sigma_0$. This paradox can be resolved only by a three-dimensional model that accounts for a tunnel of finite length. However, (20)–(22) are good approximations in the neighborhood of the tunnel. From (20)–(22), the mean stress is

$$\frac{1}{3} \text{tr} \mathbf{T} = -\frac{2}{3}(1 + \nu_u)\sigma_0. \quad (23)$$

The initial condition for the pore pressure upon rapid introduction of the tunnel is obtained from (10). At $t = 0$, before there has been any time to allow fluid flow, the change of fluid content must be zero. Therefore, from (10) and (23),

$$p(r, 0) = p_0 = B \frac{2}{3}(1 + \nu_u)\sigma_0. \quad (24)$$

Thus, introduction of the tunnel induces a pore pressure p_0 that lies between hydrostatic and lithostatic. As an illustration, consider typical properties for sedimentary rocks: $\phi_0 = 0.2$, $\gamma_f = 1.0 \times 10^3 \text{ kg/m}^3$, $\gamma_s = 2.6 \times 10^3 \text{ kg/m}^3$, $\nu_u = 0.3$, $B = 0.8$. These

parameters yield a hydrostatic pressure of $(0.98 \times 10^4)d$ Pa (with d in m), an initial pressure of $p_0 = (1.55 \times 10^4)d$ Pa, and a lithostatic pressure of $\sigma_0 = (2.23 \times 10^4)d$ Pa. This situation develops because, in the absence of the tunnel, the solid skeleton must support its own buoyant weight. When rock is removed, the increased load due to the presence of the tunnel is initially born principally by the fluid. The fluid pressure then relaxes by Darcy flow toward the tunnel, and the load is transferred from the fluid to the solid skeleton.

The pressure field corresponding to the aforementioned sequence is governed by (19) along with the initial condition (24) and boundary conditions

$$p(a, t) = 0, \quad (25)$$

$$\lim_{r \rightarrow \infty} p(r, t) = p_0. \quad (26)$$

Equation (25) simply states that fluid is free to flow to the “drained” face of the tunnel, which is maintained at zero (atmospheric) pressure.

The solution to (19) and (24)–(26) is well known (*e.g.*, [24]):

$$\frac{p}{p_0} = -\frac{2}{\pi} \int_0^\infty \exp(-u^2 t_*) \frac{J_0(ur_*)Y_0(u) - Y_0(ur_*)J_0(u)}{J_0^2(u) + Y_0^2(u)} \frac{du}{u}, \quad (27)$$

where $r_* = r/a$, $t_* = ct/a^2$, and $J_0(x)$ and $Y_0(x)$ are zero-order Bessel functions of the first and second kind, respectively. The flux at the tunnel wall follows immediately from Darcy’s law:

$$q_*(1, t_*) = -\frac{4}{\pi} \int_0^\infty \frac{\exp(-u^2 t_*)}{J_0^2(u) + Y_0^2(u)} \frac{du}{u}, \quad (28)$$

where q_* is a dimensionless flux, normalized by the reference flux $q_0 = p_0 k / \mu a$. Note that the sign of the flux is negative because it is in the $-r$ direction. The integral in (28) is difficult to evaluate accurately for very small or very large values of the dimensionless time, t_* . It is convenient, then, to appeal to the asymptotic expansion for small time:

$$\lim_{t_* \rightarrow 0} q_*(1, t_*) = -\frac{1}{\sqrt{\pi}} t_*^{-1/2} - \frac{1}{2} + \frac{\sqrt{\pi}}{4} t_*^{1/2} - \frac{1}{8} t_* + \dots, \quad (29)$$

and that for large time:

$$\lim_{t_* \rightarrow \infty} q_*(1, t_*) = -\frac{2}{\ln(4t_*) - 2\gamma} + \frac{2\gamma}{[\ln(4t_*) - 2\gamma]^2} + \dots, \quad (30)$$

where $\gamma = 0.57722$ is Euler’s constant. Equations (28)–(30) are shown in Figure 18. Note, in particular, that the flux falls off rapidly at early time, and changes slowly for $t_* > 10$.

It is also of interest to evaluate the cumulative flux, Q_* :

$$Q_* = \int_0^{t_*} q_*(1, \varsigma) d\varsigma, \quad (31)$$

where Q_* is normalized by $k p_0 a / \mu c$. For early time, (31) can be evaluated explicitly; from (29),

$$Q_* = -\frac{2}{\sqrt{\pi}} t_*^{1/2} - \frac{1}{2} t_* + \frac{\sqrt{\pi}}{6} t_*^{3/2} - \frac{1}{16} t_*^2 + \dots \quad (32)$$

A plot of the cumulative flux is shown in Figure 19. Note again that, because the flux changes slowly at late time, the cumulative flux grows nearly linearly.

4.2.4 Application to the moisture release experiments

The above model is now evaluated for properties typical of WIPP salt and for the conditions appropriate to the moisture release experiments in Rooms A1 and B. The parameters used are summarized in Table 1. Measured permeabilities in the WIPP salt are highly variable, so that k is left unconstrained; the sensitivity of the predicted flux to the permeability will become apparent. The elastic moduli for water and salt are well known. A typical value of 0.001 is used for the porosity. The viscosity of pure water at 20 °C suffices for the order-of-magnitude calculations presented here. The effective radius of the tunnel, $a = 3.5$ m, yields the same perimeter as a drift 5.5 m (18 ft) square. In this case, the ambient pressure is taken to be hydrostatic, and is calculated for $d = 600$ m.

Table 1: Model Parameters.

Material Property		Units
Permeability (k)	variable	m^2
Porosity (ϕ_0)	0.001	
Fluid bulk modulus (K_f)	2.0	GPa
Shear modulus (G)	12.0	GPa
Poisson's ratio (ν)	0.25	—
Drained bulk modulus (K)	20.0	GPa
Viscosity (μ)	1.0×10^{-3}	$\text{Pa}\cdot\text{s}$
<hr/>		
Tunnel radius (a)	3.5	m
Ambient pressure (p_0)	5.9	MPa
<hr/>		
Diffusivity (c)	$(3.6 \times 10^{13})k$	m^2/s
Characteristic time (a^2/c)	$(3.4 \times 10^{-13})/k$	s
Reference flux ($k p_0 / \mu a$)	$(1.7 \times 10^9)k$	m/s

The time between the mining of Room A1 and the initiation of the brine migration experiments is about 6 months; that for Room B is about 10 months. These times correspond to dimensionless times of $4.7 \times 10^{19} k$ and $7.9 \times 10^{19} k$, respectively. Tables 2 and 3 show the dimensionless flux, q_* , and dimensional flux, q , for a range of permeabilities, at times of 6 and 10 months.

If one assumes that the heater holes merely intercept the established flow to the drift, one can calculate the mass flux based on an appropriate area. Tables 2 and 3 show the mass flux, in g/day, based on the cross-sectional area of the holes (0.46 m^2 , designated A_1), and based on the vertical area (7.4 m^2 , designated A_2). A mass flux of the order of 10 g/day, as observed prior to turning on the heaters, is obtained for permeabilities in the range of 10^{-20} – 10^{-18} m^2 (or 10^{-8} – 10^{-6} darcy). These values are in the middle of the range of permeabilities estimated from various tests on WIPP salt [27, 28]. Note also that the fluxes predicted at 10 months are only about 10% smaller than those predicted at 6 months. This, too, is consistent with the field observations, which show only a slight decrease in the flow rate over the first eight months of operation.

Table 2: Calculated Flux, $t = 6$ mos. (Room A1).

$k (\text{m}^2)$	$k (\text{darcy})$	q_*	$q (\text{m/s})$	$\rho A_1 q (\text{g/day})$	$\rho A_2 q (\text{g/day})$
10^{-17}	10^{-5}	0.285	4.84×10^{-9}	190	3200
10^{-18}	10^{-6}	0.421	7.16×10^{-10}	28	450
10^{-19}	10^{-7}	0.584	9.93×10^{-11}	3.9	63
10^{-20}	10^{-8}	1.206	2.05×10^{-11}	0.81	13
10^{-21}	10^{-9}	3.023	5.14×10^{-12}	0.20	3.3

Table 3: Calculated Flux, $t = 10$ mos. (Room B).

$k (\text{m}^2)$	$k (\text{darcy})$	q_*	$q (\text{m/s})$	$\rho A_1 q (\text{g/day})$	$\rho A_2 q (\text{g/day})$
10^{-17}	10^{-5}	0.265	4.50×10^{-9}	180	2900
10^{-18}	10^{-6}	0.380	6.46×10^{-10}	26	420
10^{-19}	10^{-7}	0.509	8.65×10^{-11}	3.4	54
10^{-20}	10^{-8}	1.006	1.71×10^{-11}	0.68	11
10^{-21}	10^{-9}	2.421	4.12×10^{-12}	0.16	2.6

The same order of magnitude brine flow estimate would have been obtained from a locally bounded domain of pores containing fluid that was at lithostatic pressure before excavation. Measurements of the pore pressure field in the neighborhood of WIPP excavations may lead to the choice of a realistic model.

4.2.5 Summary

The background moisture release rates that were observed in WIPP moisture release experiments may be due to a Darcy flow mechanism. A highly idealized Darcy flow model has been evaluated in order to provide an order-of-magnitude estimate of the brine flow expected in the neighborhood of the heater holes in Rooms A1 and B. The model considers Darcy flow due to the introduction of a zero-pressure face by the mining of the drifts. Calculations based on one-dimensional, radial flow to a circular tunnel suggest that mass flow rates of the order of 10 g/day into the heater holes, as observed, could be obtained from salt with permeability in the range of 10^{-20} – 10^{-18} m² (or 10^{-8} – 10^{-6} darcy). These values are, in fact, representative of the permeabilities estimated for WIPP salt to date [27, 28]. Thus, it seems plausible that the background flow observed in the holes before turning on the heaters may be due to this Darcy flow mechanism.

This conclusion does not constitute a test of critical assumptions in the model, *i.e.*, interconnected porosity throughout the host rock formation and hydrostatic pore pressure before excavation. The model was chosen for its closed-form solution that facilitated the calculations.

It is worth noting that certain expectations about brine flow in the field test were predicated on experience with laboratory experiments such as Salt Block II. However, the sample in Salt Block II was under essentially *zero* hydrostatic head in the laboratory, while the far-field pressure near the *in situ* experiment is very large. Thus, the brine flow in the laboratory may have been driven principally by the relative thermal expansion of the brine and salt [25, 26], while this effect may be overwhelmed by the hydrostatically-driven flow in the field setting.

4.3 Pore pressure profiles near WIPP rooms A1 and B

4.3.1 Introduction

Calculations of the pore pressure field in the neighborhood of WIPP rooms can provide physical insight. The results may suggest the size of a domain of interconnected porosity that is needed to account for the measured quantities of released moisture. The results can also provide guidance for the design of meaningful pore pressure measurements that could provide critical tests of the mechanistic assumptions that have been made. In particular, the relaxation of the pre-excavation pore pressure by Darcy flow to the mined face is evaluated using the idealized model that was summarized in Subsection 4.2.

4.3.2 Pressure profile

The solution for the pressure field due to the introduction of a zero-pressure, circular tunnel at time $t = 0$ in an unbounded region at constant initial pressure p_0 is given by (27).

The integral in equation (27) is difficult to evaluate accurately for small values of the dimensionless time, $t_* = ct/a^2$. Thus, it is convenient to use the asymptotic solution

$$\begin{aligned} \frac{p}{p_0} = & 1 - \frac{1}{\sqrt{r_*}} \operatorname{erfc} \frac{r_* - 1}{2\sqrt{t_*}} - \frac{(r_* - 1)\sqrt{t_*}}{r_*^{3/2}} \operatorname{i erfc} \frac{r_* - 1}{2\sqrt{t_*}} \\ & - \frac{(9 - 2r_* - 7r_*^2)}{32r_*^{5/2}} i^2 \operatorname{erfc} \frac{r_* - 1}{2\sqrt{t_*}} + \dots \end{aligned} \quad (33)$$

Profiles computed from equations (27) and (33) are shown in Figure 20 for $t_* = 0.01, 0.1, 0.5, 1.0, 5.0, 10.0$, and 50.0 . The first three are based on the early-time expansion (33); the last four are based on the integral solution (27).

4.3.3 Application to rooms A1 and B

Table 1 shows material properties estimated for WIPP salt and brine and other necessary model parameters. The permeability is left unspecified because field measurements have shown it to be highly variable.

The mining of Room A1 was initiated on about October 1, 1984; Room B was started on about June 1, 1984. Thus, on August 1, 1986, the mined faces were about 22 and 26 months old, respectively. Previous consideration of the brine flux into the unheated boreholes (Section 4.2) suggested that the effective permeability is less than 10^{-20} m^2 , or 10 nanodarcy. For the elastic properties given in Table 1 and an effective tunnel radius of 3.5 m, the dimensionless ages of Rooms A1 and B are then 1.7 and 2.0, respectively.

Figure 21 shows the radius at which the pressure has fallen to 50% and 75% of its initial value, plotted against dimensionless time. For the above example, the pressure is still at 75% of its initial value at r_* of about 3, or only about 7 meters away from the tunnel wall. Table 4 shows the dimensionless radii at which the pressure in this example calculation has fallen to 50% (r_{50}), 75% (r_{75}), and 90% (r_{90}) of its initial value for $t_* = 1.7$ and 2.0 . Also included are the distances from the tunnel wall corresponding to these radii for $a = 3.5$ m.

Table 4: Radius at which pore pressure has relaxed to 50%, 75%, and 90% of its initial value for $k = 10^{-20} \text{ m}^2$. Figures in parentheses are corresponding dimensional distances from the tunnel wall, $(r_* - 1)a$, for $a = 3.5 \text{ m}$.

	Room A1	Room B
	$t = 22 \text{ mo.}$	$t = 26 \text{ mo.}$
	$t_* = 1.7$	$t_* = 2.0$
r_{50}	1.8 (2.8 m)	1.9 (3.2 m)
r_{75}	2.8 (6.3 m)	3.0 (7.0 m)
r_{90}	4.2 (11.2 m)	4.5 (12.2 m)

4.3.4 Summary

Field experiments have been proposed to evaluate the relaxation of the hydrostatic pore pressure in the neighborhood of the WIPP facility. Design considerations require estimates of the radius to which the relaxation has proceeded to date. The diffusion model developed previously, which was shown to provide a reasonably good representation of moisture release data, has been used to calculate the penetration depth over the two years since the mining of Rooms A1 and B. For a permeability of 10^{-20} m^2 (10 nanodarcy), the pore pressure is shown to remain at 75% of its initial value only 7 meters away from the drift wall. A lower effective permeability yields a correspondingly shorter penetration depth for the relaxation front. These results are very encouraging for the execution of an experiment designed to monitor the pore pressure, because the drilling depths required are easily attained.

4.4 Effect of temperature-dependent viscosity

4.4.1 Introduction

After initiation of heating, the measured moisture release rates increased. For the boreholes with 1500 W heaters in Room B, the increase was large and persistent. Temperature-dependent viscosity may provide an explanation of this observation. It is therefore useful to estimate the magnitude of increased flow due solely to the temperature dependence of brine viscosity in the model. The model does not address the flow due to differential thermal expansion of the brine and salt [*e.g.*, 25, 26].

4.4.2 Temperature-dependent viscosity

Previous calculations suggested that the measured flow of brine in rooms A1 and B can be accounted for by Darcy flow due to the far-field, hydrostatic pressure at the

repository depth. The permeability inferred is of the order of 10^{-20} m^2 (10 nanodarcy), which is consistent with independent estimates [27, 28]. The isothermal problem takes the form of a simple diffusion equation for the fluid pressure, with a region initially at uniform pressure that relaxes by flow to a zero-pressure, circular, internal surface. Because the fluid diffusivity is inversely proportional to the fluid viscosity, and the viscosity is quite sensitive to temperature, the nonisothermal problem introduces the need to solve for the temperature field simultaneously. The diffusion equation for the pressure field is then coupled to the temperature field through the fluid diffusivity, and, of course, becomes nonlinear.

The model problem considered takes the following form. The temperature field is governed by

$$\frac{\partial \theta}{\partial t} - \frac{\kappa}{r} \frac{\partial}{\partial r} \left(r \frac{\partial \theta}{\partial r} \right) = 0, \quad (34)$$

with initial and boundary conditions given by

$$\theta(r, 0) = \theta_0, \quad (35)$$

$$\frac{\partial \theta}{\partial r}(a, t) = -\frac{q_0}{K}, \quad (36)$$

$$\lim_{r \rightarrow \infty} \theta(r, t) = \theta_0, \quad (37)$$

where θ is the temperature, κ is the thermal diffusivity, a is the borehole radius, θ_0 is the ambient temperature, q_0 is the heat flux delivered to the borehole wall, and K is the thermal conductivity. The fluid pore pressure field is governed by

$$\frac{\partial p}{\partial t} - \frac{1}{r} \frac{\partial}{\partial r} \left[c(\theta) r \frac{\partial p}{\partial r} \right] = 0, \quad (38)$$

with initial and boundary conditions given by

$$p(r, 0) = p_0, \quad (39)$$

$$p(a, t) = 0, \quad (40)$$

$$\lim_{r \rightarrow \infty} p(r, t) = p_0, \quad (41)$$

where p is the pressure, $c(\theta)$ is the temperature-dependent fluid diffusivity, and p_0 is the intial value of the pressure.

The model problem, then, assumes a long, cylindrical borehole in an initially isothermal region (35), to which is delivered a constant heat flux (36). Due to the sudden introduction of the borehole, the pore pressure initially takes a uniform value, p_0 , between hydrostatic and lithostatic (39). Water is free to flow to the borehole, the boundary of which remains at zero excess pressure (40).

The fluid diffusivity may be written in a form that reveals the role of the temperature-dependent viscosity:

$$c(\theta) = c_0 \frac{\mu_0}{\mu(\theta)}, \quad (42)$$

where c_0 and μ_0 are reference values of the diffusivity and viscosity, respectively. The empirical form used for the viscosity of a saturated brine is

$$\mu(\theta) = (2.965 \times 10^{-3}) \exp(-0.0214\theta) \text{ Pa} \cdot \text{s}, \quad (43)$$

where the temperature, θ , is in $^{\circ}\text{C}$.

4.4.3 Numerical solution

The foregoing system of equations was solved numerically by the method of lines, employing modifications to a computer code provided by M. R. Baer (1513).

The far-field boundary conditions (37, 41) are difficult to treat numerically. Thus, it is convenient to introduce the following change of variables:

$$\eta = 1 - \exp \left[-\varsigma \left(\frac{r}{a} - 1 \right) \right], \quad (44)$$

where ς is a constant. Clearly, η has the attractive properties that $\eta = 0$ at $r = a$ and $\eta = 1$ as $r \rightarrow \infty$. The “stretch factor” ς can be chosen appropriately for the length scale over which the fields vary at a given time plane of interest. For example, consider a discretization of the region from $\eta = 0$ to $\eta = 1$ into 40 equal segments. The 41st node is located at $\eta = 1$, which corresponds to $r \rightarrow \infty$. The 40th node is at $\eta = 0.975$. For $\varsigma = 10$, this corresponds to $r/a = 1.37$; for $\varsigma = 1$, $r/a = 4.69$; for $\varsigma = 0.1$, $r/a = 37.89$; for $\varsigma = 0.01$, $r/a = 369.89$.

Under the change of variable, (34)–(37) become

$$\frac{\partial \theta}{\partial t} - \frac{\kappa \varsigma^2}{a^2} \frac{1-\eta}{\varsigma - \ln(1-\eta)} \frac{\partial}{\partial \eta} \left\{ [\varsigma - \ln(1-\eta)](1-\eta) \frac{\partial \theta}{\partial \eta} \right\} = 0, \quad (45)$$

$$\theta(\eta, 0) = \theta_0, \quad (46)$$

$$\frac{\partial \theta}{\partial \eta}(0, t) = -\frac{q_0 a}{K \varsigma}, \quad (47)$$

$$\theta(1, t) = \theta_0, \quad (48)$$

and (38)–(41) become

$$\frac{\partial p}{\partial t} - \frac{\varsigma^2}{a^2} \frac{1-\eta}{\varsigma - \ln(1-\eta)} \frac{\partial}{\partial \eta} \left\{ c(\theta) [\varsigma - \ln(1-\eta)](1-\eta) \frac{\partial p}{\partial \eta} \right\} = 0, \quad (49)$$

$$p(\eta, 0) = p_0, \quad (50)$$

$$p(0, t) = 0, \quad (51)$$

$$p(1, t) = p_0. \quad (52)$$

An exact solution to (34)–(37) is well known [29, p. 335]; the numerical scheme was tested against it and proved to be very accurate (Figure 22). An analytical solution to (38)–(41) in the isothermal case ($c = \text{constant}$) is also known (Section 4.2.3, Eq. 27), and provides an additional check on the numerical results.

4.4.4 Test problem

The parameters used in the sample calculation are summarized in Table 5.

Table 5: Model Parameters.

Parameter		Units
Borehole radius (a)	0.381	m
Heat flux (q_0)	202.0	W/m ²
Thermal conductivity (K)	4.5	W/m/°C
Thermal diffusivity (κ)	2.41×10^{-6}	m ² /s
Ambient temperature (θ_0)	20.0	°C
Permeability (k)	1.0×10^{-20}	m ²
Fluid diffusivity* (c_0)	3.6×10^{-7}	m ² /s
Fluid viscosity* (μ_0)	1.93×10^{-3}	Pa·s
Initial pressure (p_0)	10.0	MPa
Stretch factor (ς)	0.1–1.0	—

*at 20 °C

The borehole radius corresponds to that of the heated holes in rooms A1 and B. For a heated length of 3.1 m (122"), the vertical surface area is 7.4 m². The 1500 W heaters used in room B then deliver a heat flux of 202 W/m². The permeability and fluid diffusivity used are of the order suggested by previous modeling of the isothermal problem (Section 4.2). The initial value of the pressure lies between hydrostatic and lithostatic (overburden) at the repository depth. The calculations were carried out using 41 nodes.

Figures 23 and 24 show temperature and pressure profiles, respectively, at 1, 10, and 100 days. Figure 25 shows the rise of the wall temperature for 100 days. The calculated wall temperature exhibits behavior qualitatively like that measured in the room B holes. However, the calculated temperature rise after 100 days is only about 45 °C, while the observed rise was approximately 70 °C. This is due to the influence of the other heaters in the room B array, which are not accounted for in the model calculation. Nonetheless, the present sample calculations are adequate to investigate the effect of temperature-dependent viscosity.

Figure 26 shows the calculated brine flux (volume flux per unit area) history in the unheated (20 °C) and heated (202 W/m²) cases for 100 days. The difference is relatively small at early time, but approaches a factor of two as the region heats and the flux falls off. For comparison, note that a collection rate of 10 g/day of pure water corresponds to a brine flux of 1.8×10^{-11} m/s over an area of 7.4 m². Figure 27 shows the increase in fluid flux relative to the isothermal case as the fluid diffusivity at the borehole wall increases. After 100 days, the value of c at 65 °C is over 2.5 times greater

than the reference (20°C) value, and the fluid flux is 1.6 times greater than in the unheated case.

Table 6 shows key results from the calculations, including the radius at which the pressure remains at 90% of its initial value.

Table 6: Calculated Borehole Temperature, Brine Flux, and Radius Where $p/p_0 = 0.9$.

Time (days)	Wall Temp ($^{\circ}\text{C}$)	Flux (m/s)	Radius Where $p/p_0 = 0.9$ (m)
1	34.3	-2.64×10^{-10}	0.78
10	48.1	-1.41×10^{-10}	1.58
100	64.5	-9.05×10^{-11}	3.97

4.4.5 Summary

The principal results of this study are:

- A numerical scheme has been implemented to treat one-dimensional, nonisothermal, radial flow in an unbounded region. The brine flow is coupled to the temperature field through a temperature-dependent fluid diffusivity. Only modest modifications are required to include in the same code the effect of differential thermal expansion [25, 26].
- Sample calculations show that the decrease in viscosity due to elevated temperature has a significant effect on the flow rate, of the order of a factor of two.
- The temperature dependence of viscosity cannot account for all of the order-of-magnitude increase in moisture release that followed the initiation of heating in room B.

4.5 Long-term, steady-state, brine flow

4.5.1 Introduction

The transient model that has been described and implemented thus far cannot be valid after very long time periods, because the assumed far-field boundary condition is no longer approximately correct as the flow propagates out to large length scales that approach the burial depth. Therefore, it is necessary to estimate the accuracy of the transient model for the time periods after excavation that are pertinent to this data analysis. For that purpose, the following simplified estimate of the steady flow into the

open WIPP facility at very long time was generated for comparison with the inflows from the transient model.

4.5.2 Steady flow to a line sink

Darcy's law is given by

$$\mathbf{q} = -\frac{k}{\mu} \nabla \Phi, \quad (53)$$

where \mathbf{q} is the fluid flux (volume rate per unit area), k is the permeability, and μ is the fluid viscosity. The potential, Φ , is defined by

$$\Phi = p + \gamma_f g z, \quad (54)$$

where p is the fluid pressure, γ_f is the fluid density, g is the acceleration due to gravity, and z is the vertical coordinate, here measured positive upward from the water table. For steady-state flow, or for an incompressible fluid in a rigid, porous matrix, substitution of (53) into the fluid mass balance yields

$$\nabla^2 \Phi = 0. \quad (55)$$

Consider the flow to a horizontal, circular tunnel of radius a , centered at depth d beneath the water table. The exact problem for the potential field is quite complex because the potential on the tunnel surface (54) varies slightly due to the change in elevation around the circumference and because the free surface will be displaced, and its location is part of the solution. However, in the present case, because the tunnel radius is very small compared to its depth, and because the flow is very weak, an approximate, but very accurate, solution can be obtained.

The potential for the flow to a tunnel of radius a in an unbounded region is well-known:

$$\Phi_1 = -\Phi_* + \frac{Q\mu}{2\pi k} \ln \left(\frac{r_1}{a} \right), \quad (56)$$

where r_1 is the radial coordinate centered on the tunnel, $Q = -2\pi a q_r(a)$ is the total flux per unit length into the tunnel (e.g., in m^2/s), and $\Phi_1(a) = -\Phi_*$ is the potential at the tunnel. A horizontal potential surface taking the value zero can be introduced by the superposition of a source of equal strength:

$$\Phi_2 = \Phi_* - \frac{Q\mu}{2\pi k} \ln \left(\frac{r_2}{a} \right), \quad (57)$$

where r_2 is the radial coordinate centered on the source. The total potential is then

$$\Phi = \Phi_1 + \Phi_2 = \frac{Q\mu}{2\pi k} \ln \left(\frac{r_1}{r_2} \right). \quad (58)$$

Equation (58) is the well-known, singular solution for the potential due to a line sink and opposing line source. It should be noted that (58) results in a *plane* surface with

$\Phi = 0$ midway between the sink and source; i.e., the model *prescribes* the location of the free surface, and does not allow for drawdown. However, this assumption can be shown to be valid for $a/d \ll 1$ and small Q . The equipotential surfaces given by (58) are shown in Figure 28, and the associated streamlines are illustrated in Figure 29.

The surface of the deep tunnel is a potential surface, but the depth to the line sink and the depth to the center of the tunnel do not coincide. However, for $a/d \ll 1$, these two length scales may be assumed equal. Thus, on the tunnel boundary, $r_1 \simeq a$. Furthermore, the distance from the opposing line source is very nearly $2d$, so that $r_2 \simeq 2d$ near the tunnel. Finally, the potential (54) at the tunnel, where the pressure vanishes ($p = 0$), is $-\Phi_*$, where Φ_* is given approximately by

$$\Phi_* = \gamma_f g d. \quad (59)$$

Substitution of these values into (58) yields

$$Q = \frac{-2\pi k \Phi_*}{\mu \ln(a/2d)}. \quad (60)$$

It can be verified that (60) is the limit, for small a/d , of the more complete solution.

Example. Consider as an example one case treated in the analysis of the transient flow (Section 4.2). Assume the following material properties:

$$k = 10^{-21} \text{ m}^2,$$

$$\mu = 10^{-3} \text{ Pa} \cdot \text{s},$$

$$\gamma_f = 10^3 \text{ kg/m}^3,$$

and a mined drift characterized by

$$a = 3.5 \text{ m},$$

$$d = 600 \text{ m}.$$

These parameters yield, from (60),

$$Q = 6.3 \times 10^{-12} \text{ m}^2/\text{s},$$

or

$$|q_r(a)| = 2.9 \times 10^{-13} \text{ m/s}.$$

The last value compares with results from the transient analysis, for identical conditions, of 5.1×10^{-12} m/s 6 months after mining and 4.1×10^{-12} m/s 10 months after mining. As expected, the estimated, steady-state flux is considerably less than the transient flux after a short time. However, the transient solution vanishes at long time. Equation (60) is compared to the late-time solution (Section 4.2, Eq. 30) in Figure 30.

4.5.3 Flow to a point sink

One might object that the model for a line sink implies that the tunnel is very long in comparison to its depth, and that the flow into a mined drift may be more closely approximated by flow to a point sink. Indeed, the length of test rooms A1 and B in the WIPP facility is $L \simeq 90$ m, so that $L/d \simeq 0.15 \ll 1$. The analysis is analogous to that already given. The potential field for a point sink and opposing point source is given by

$$\Phi = \frac{Q\mu}{4\pi k} \left(\frac{1}{r_2} - \frac{1}{r_1} \right), \quad (61)$$

where $Q = -4\pi a^2 q_r(a)$ is the total flux into the sink (e.g., in m^3/s), and a is the radius of the “effective” spherical source. Again, at the boundary of the spherical cavity, $r_1 \simeq a$, $r_2 \simeq 2d$, and $\Phi \simeq -\Phi_*$, so that (61) gives, approximately,

$$Q = \frac{4\pi k a \Phi_*}{\mu(1 - a/2d)}. \quad (62)$$

Example. Consider the sample calculation parallel to that treated for the line sink. Rooms A1 and B are about 91.4 m (300 ft) long, and 5.5 m (18 ft) square, which yields a surface area of about $2.1 \times 10^3 \text{ m}^2$, or an equivalent sphere of radius

$$a = 12.9 \text{ m}.$$

Substitution into (62) yields, for $k = 10^{-21} \text{ m}^2$,

$$Q = 9.6 \times 10^{-10} \text{ m}^3/\text{s},$$

or

$$|q_r(a)| = 4.6 \times 10^{-13} \text{ m/s}.$$

This represents 1.6 times the flow predicted for the plane flow to a line sink, indicating that the weaker flow to the point sink is compensated by the greater surface area accounted for.

4.5.4 Summary and conclusions

The early-time, transient analysis that was developed and applied in Sections 4.2, 4.3, and 4.4 is appropriate for the short times after excavation that characterize WIPP *in situ* tests. The transient flux does not reach the steady state value until more than 5000 years after excavation has taken place.

The analysis presented here provides a first estimate of the very-long-term, steady, Darcy flow into a mined cavity due to the far-field, hydrostatic head. For a configuration representative of Rooms A1 and B in the WIPP facility, the analysis predicts flow of the order of $10^{-13}\text{--}10^{-12} \text{ m}^3/\text{s}$ per square meter of wall surface for a permeability of 10^{-21} m^2 (1 nanodarcy). This is approximately an order of magnitude less than the flow predicted for the same conditions using a transient model appropriate at early

time. The transient model, in contrast, employed far-field boundary conditions that are incorrect after long time, and consequently predicts that the flow vanishes entirely.

Figure 30 shows that the late-time, transient flux does not reach the steady-state prediction for $a/d = 0.00583$ until a dimensionless time of about 5×10^4 . Even for a relatively high permeability of 10^{-19} m^2 (100 nanodarcy), this is a real time of about 5400 years, and is inversely proportional to the permeability. Thus, it appears that, for any time of practical interest, the early-time, transient analysis is appropriate.

It is emphasized that the simple analysis presented here invokes the very unrealistic assumption that the entire region is comprised of an isotropic, homogeneous, porous medium with a permeability like that of the salt. However, the flow is limited principally by the near-field permeability, because the flux falls off rapidly away from the mined surface. The results, then, are expected to be rather insensitive to the far-field properties.

5 Conclusions and Recommendations

Significant brine transport can occur to unheated boreholes in the WIPP. This observation highlights the need for an isothermal model of brine movement in the WIPP host rock bedded salt of the Salado formation.

Better models are also needed for thermally induced brine transport in the Salado. Cumulative quantities of water from heated WIPP test boreholes have exceeded previous model predictions by about two orders of magnitude.

Results from *in situ* brine transport tests in domal salt (salt formations resulting from diapirism) are not necessarily applicable to bedded salt. Brine inflows measured in the Asse mine (domal salt in the Federal Republic of Germany) brine migration tests were much smaller than the inflows that were measured in the WIPP (bedded salt) moisture release experiments, even after differences in borehole wall area and water content of salt are taken into account.

The partial pressure of water vapor is not a controlling variable for brine transport to the heated boreholes in Room A1. Therefore, vapor phase transport of water is not a likely mechanism to explain our heated borehole water collection rates.

A Darcy flow model is promising for mechanistic analyses of the WIPP test results for unheated boreholes. Our water collection data for unheated boreholes agreed reasonably well with the brine inflows that were calculated with this model. Agreement was attained using permeability and porosity values that are estimated from *in situ* tests in the WIPP host rock. It was also shown that the WIPP experiments are well within the transient stage of this model. The model also predicts pore pressure gradients that are nearly totally contained within a few meters of WIPP excavations. Therefore, the brine source could be locally bounded and still yield flows that fit this model.

Additional model development is needed for further analyses of the heated borehole results. The temperature dependence of viscosity in our current Darcy flow model is inadequate to account for the large water collection rates that were observed after Room B heaters were turned on.

Experiments are needed to test some of our current hypotheses and assumptions concerning brine transport to unheated WIPP excavations. Experiments to test the following parameters are recommended:

- Time — to several months or years
- Scale —
 - borehole diameter from 5" to 36"
 - room-size excavation
- Water vapor pressure — saturated to low values controlled with nitrogen gas flow
- Salt composition and structure — test compositionally and structurally different host rock strata

Pore pressure measurements at intervals out to several meters away from WIPP excavations are also recommended. These measurements are intended to test model predictions of the pore pressure field; they may also yield an approximate value for the pre-excavation pore pressure. Knowledge of the pre-excavation pore pressure and the extent of the pore pressure field may lead to a better physical picture of the brine sources for flow into the WIPP. For example, pre-excavation pore fluids at lithostatic pressure would suggest that the source of brine may be locally bounded within the Salado formation.

WIPP hydrologic and disturbed zone characterization studies can also contribute to our understanding of brine transport to WIPP excavations. These studies may reveal aspects of the fluid transmissivity and general hydrologic characteristics of WIPP host rock that control the movement of naturally occurring brine.

6 References

1. S. R. Black, R. S. Newton, and D. K. Shukla, eds., Results of Site Validation Experiments, Vol. II, Supporting Document 10, Brine Content of Facility Interval Strata, U. S. Department of Energy, Waste Isolation Pilot Plant, March 1983.
2. Panel on the Waste Isolation Pilot Plant (WIPP), National Research Council, Review of the Scientific and Technical Criteria for the Waste Isolation Pilot Plant, **DOE/DP/48015-1**, National Academy Press, Washington, D. C., 1984, pp. 34-37.
3. R. L. Bradshaw and W. C. McCain, eds., Project Salt Vault: A Demonstration of the Disposal of High-Activity Solidification Wastes in Underground Salt Mines, **ORNL-4555**. Oak Ridge National Laboratory, April 1971.
4. S. J. Lambert and H. C. Shefelbein, A Strategy for Investigation of Fluid Migration in Evaporites (Waste Isolation Pilot Plant-WIPP), **SAND79-1889**, Sandia National Laboratories, March 1980.
5. H. C. Shefelbein, Brine Migration: A Summary Report, **SAND82-0152**, Sandia National Laboratories, September 1982.
6. R. I. Ewing, Test of a Radiant Heater in the Avery Island Salt Mine, **SAND81-1305**, Sandia National Laboratories, November 1981.
7. W. B. Krause and P. F. Gnirk, Domal Salt Brine Migration Experiments at Avery Island, Louisiana, Advances in the Science and Technology of the Management of High Level Nuclear Waste, prepared for the Office of Nuclear Waste Isolation, Battelle Memorial Institute, Columbus, OH, July 1981.
8. W. B. Krause and L. L. Van Sambeek, Avery Island Test Site Procedure for Installation and Operation of Brine Movement Experiments and Prototype Test Site, **ONWI/SUB-79/E512-02200/10**, prepared by RE/SPEC, Inc., Rapid City, SD, RSI-0090, for Office of Nuclear Waste Isolation, Battelle Memorial Institute, Columbus, OH, 1979
9. W. B. Krause, L. L. Van Sambeek, and R. G. Stickney, *In Situ* Brine Migration Experiments at the Avery Island Salt Mine, Heat Transfer in Nuclear Waste Disposal, HTD-Vol. II, presented at the ASME Winter Annual Meeting, Chicago, IL, November 16-21, 1980.
10. R. I. Ewing, Preliminary Moisture Release Experiment in a Potash Mine in South-eastern New Mexico, **SAND81-1318**, Sandia National Laboratories, November 1981.

11. Stein, C. L., and Krumhansl, J. L., Chemistry of Brines in Salt from the Waste Isolation Pilot Plant (WIPP) Facility, Southeastern New Mexico: a Preliminary Investigation, **SAND85-0897**, Sandia National Laboratories, March 1986.
12. T. Rothfuchs, D. Lubker, A. Coyle, and H. Kalia, Nuclear Waste Repository Simulation Experiments, Asse Salt Mine, Federal Republic of Germany: Annual Report 1983, prepared for Office of Nuclear Waste Isolation, Battelle Memorial Institute, Columbus, OH, October 1984.
13. A. J. Coyle, J. Eckert, and H. Kalia, Brine Migration Test Report: Asse Salt Mine, Federal Republic of Germany, **BMI/ONWI-624**, prepared for Office of Nuclear Waste Isolation, Battelle Memorial Institute, Columbus OH, January 1987.
14. E. J. Nowak, Test Plan: Moisture Release Experiment for Rooms A1 and B, Sandia National Laboratories, March 1985.
15. R. V. Matalucci, C. L. Christensen, T. O. Hunter, M. A. Molecke, and D. E. Munson, Waste Isolation Pilot Plant (WIPP) Research and Development Program: *In Situ* Testing Plan, **SAND81-2628**, Sandia National Laboratories, March 1982.
16. R. V. Matalucci and D. E. Munson, Planning, Development, and Organizing *In Situ* Tests for the Waste Isolation Pilot Plant (WIPP), Proceedings Second Conference on the Mechanical Behavior of Salt, March 1982.
17. M. A. Molecke, WIPP Waste Package Testing on Simulated DHLW: Emplacement, in Scientific Basis for Nuclear Waste Management VIII, Materials Research Society Symposium, Vol. 44, Boston, MA, November 1984.
18. E. J. Nowak, Preliminary Results of Brine Migration Studies in the Waste Isolation Pilot Plant (WIPP), **SAND86-0720**, Sandia National Laboratories, May 1986.
19. E. J. Nowak, Brine Influx Rates from Host Rock Salt for Design Evaluation Calculations, Memorandum of Record, October 31, 1986.
20. Rice, J. R., and Cleary, M. P., Some basic stress-diffusion solutions for fluid-saturated elastic porous media with compressible constituents, *Reviews of Geophysics and Space Physics*, **14** (1976), 227-241.
21. Biot, M. A., General theory of three dimensional consolidation, *Journal of Applied Physics*, **12** (1941), 155-164.
22. McTigue, D. F., A Linear Theory for Porous Thermoelastic Materials, **SAND85-1159**, Sandia National Laboratories, September, 1985.

23. Bredehoeft, J. D., Pore fluid regime - WIPP repository, memo to Members of the WIPP Panel, February 27, 1986.
24. Crank, J., *The Mathematics of Diffusion*, Clarendon Press, Oxford, 1979.
25. McTigue, D. F., Brine flow to a heated borehole, memo to C. L. Stein, August 13, 1984.
26. McTigue, D. F., Further calculations for brine flow to a heated borehole, memo to C. L. Stein, September 13, 1984.
27. Peterson, E., Lagus, P., Brown, J., and Lie, K., WIPP Horizon *In Situ* Permeability Measurements, Final Report, SAND85-7166, prepared for Sandia National Laboratories by S-Cubed, La Jolla, CA, January, 1985.
28. Stormont, J. C., Peterson, E. W., and Lagus, P. L., Summary of WIPP Facility Horizon Flow Measurements Through 1986, SAND87-0176, Sandia National Laboratories, in preparation.
29. Carslaw, H. S., and Jaeger, J. C., *Conduction of Heat in Solids*, Oxford University Press, Oxford, 1959.

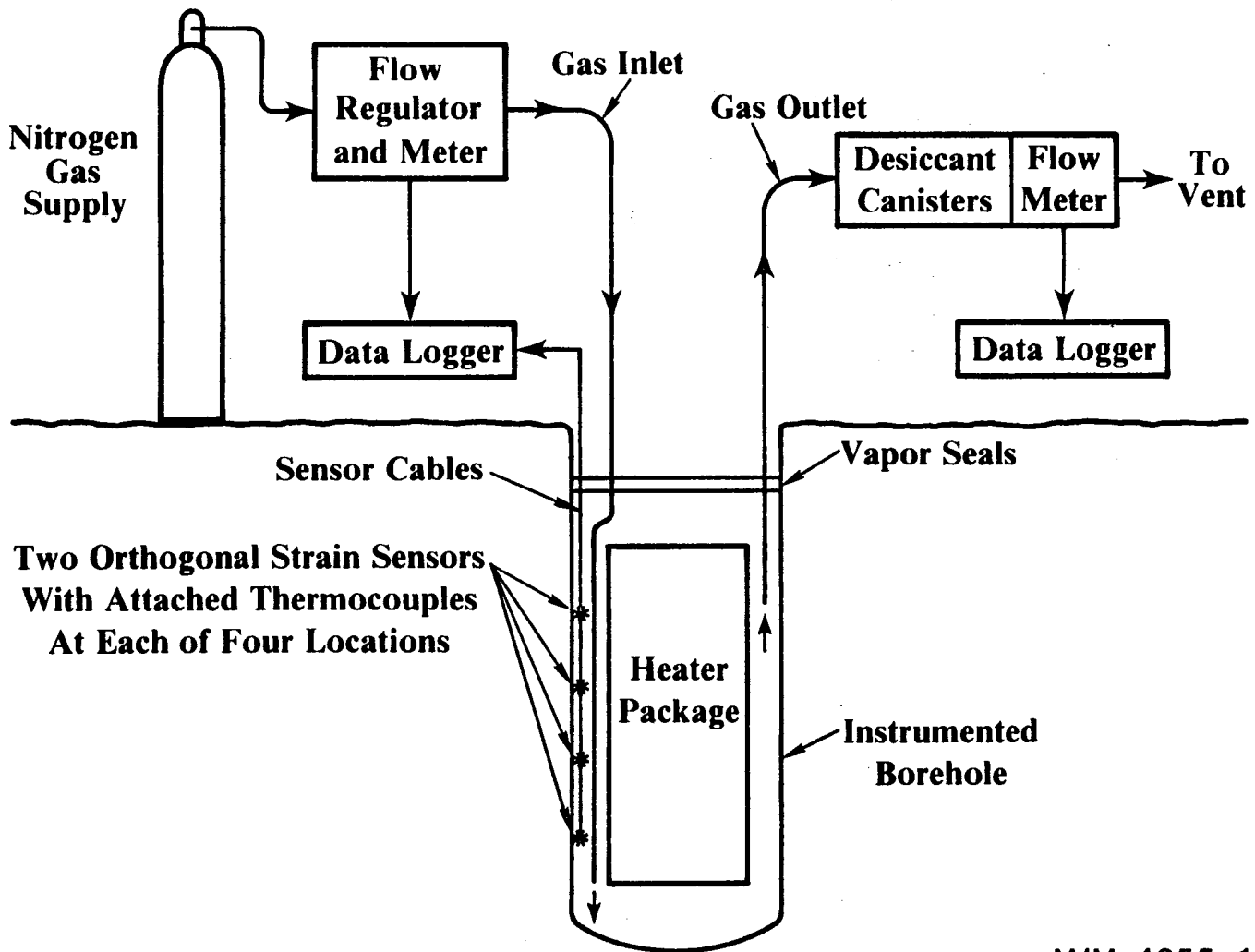


Figure 1: Schematic diagram of the experimental system for each borehole.

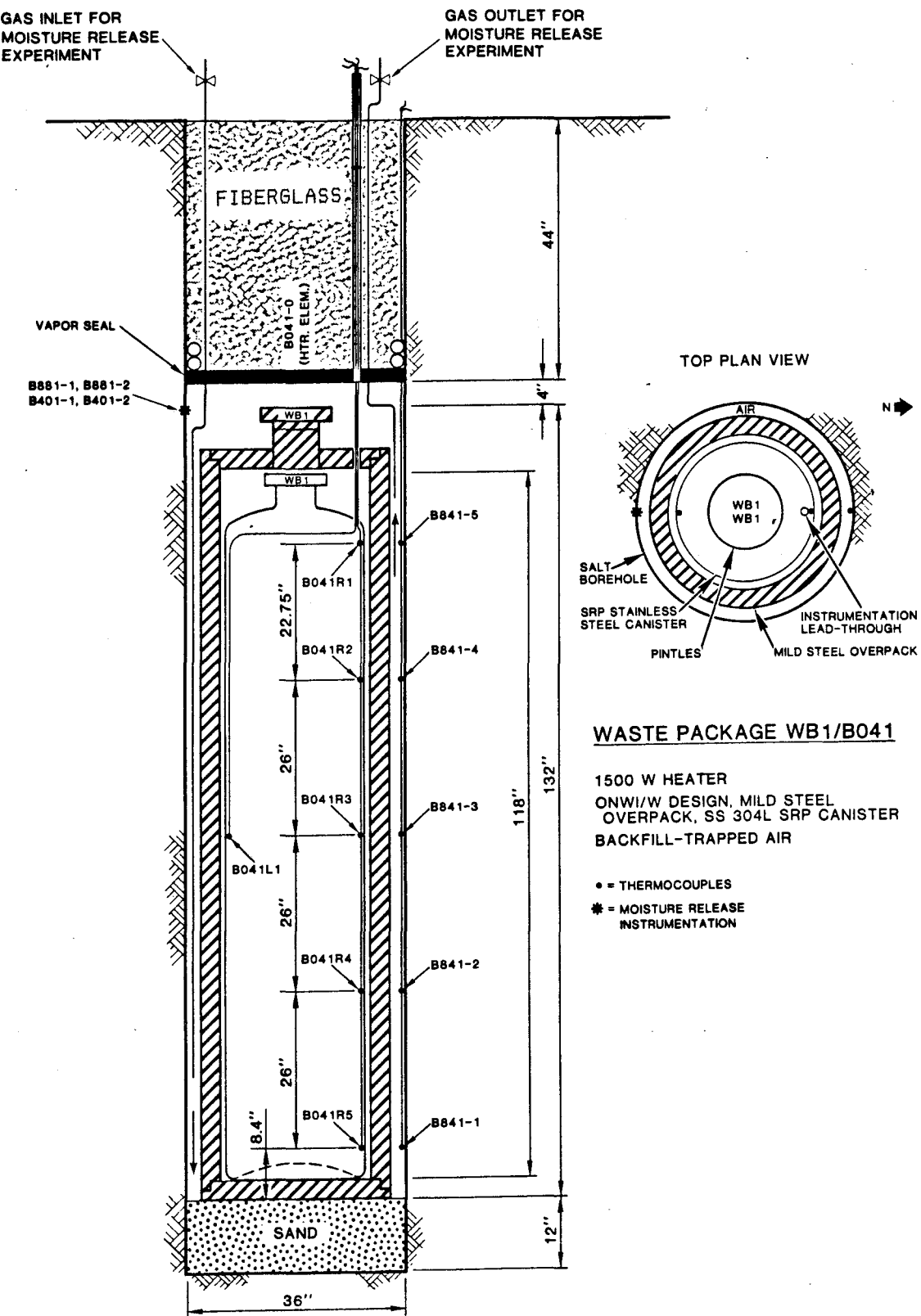


Figure 2: Instrumentation and waste package emplacement WB1.

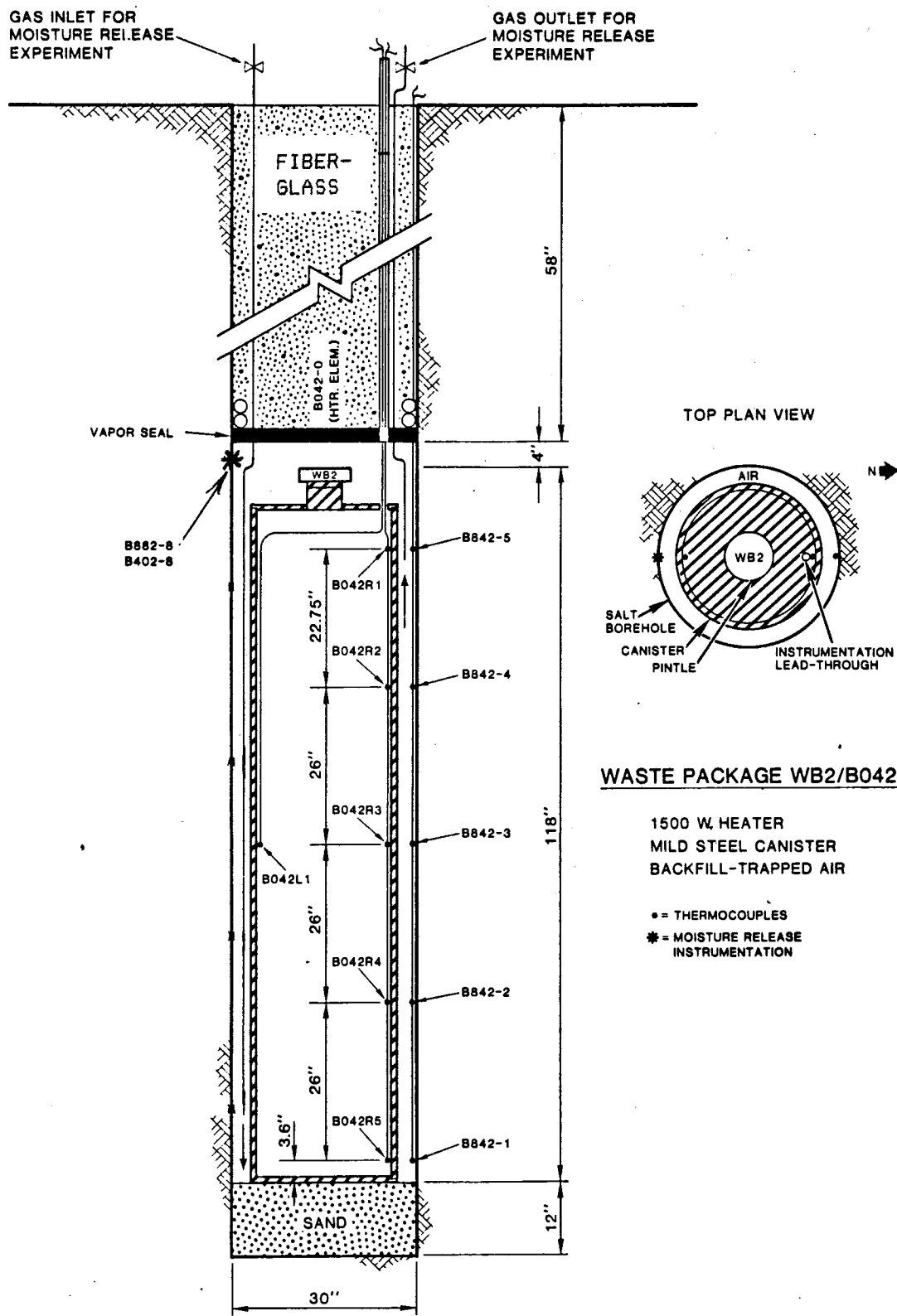


Figure 3: Instrumentation and waste package emplacement WB2.

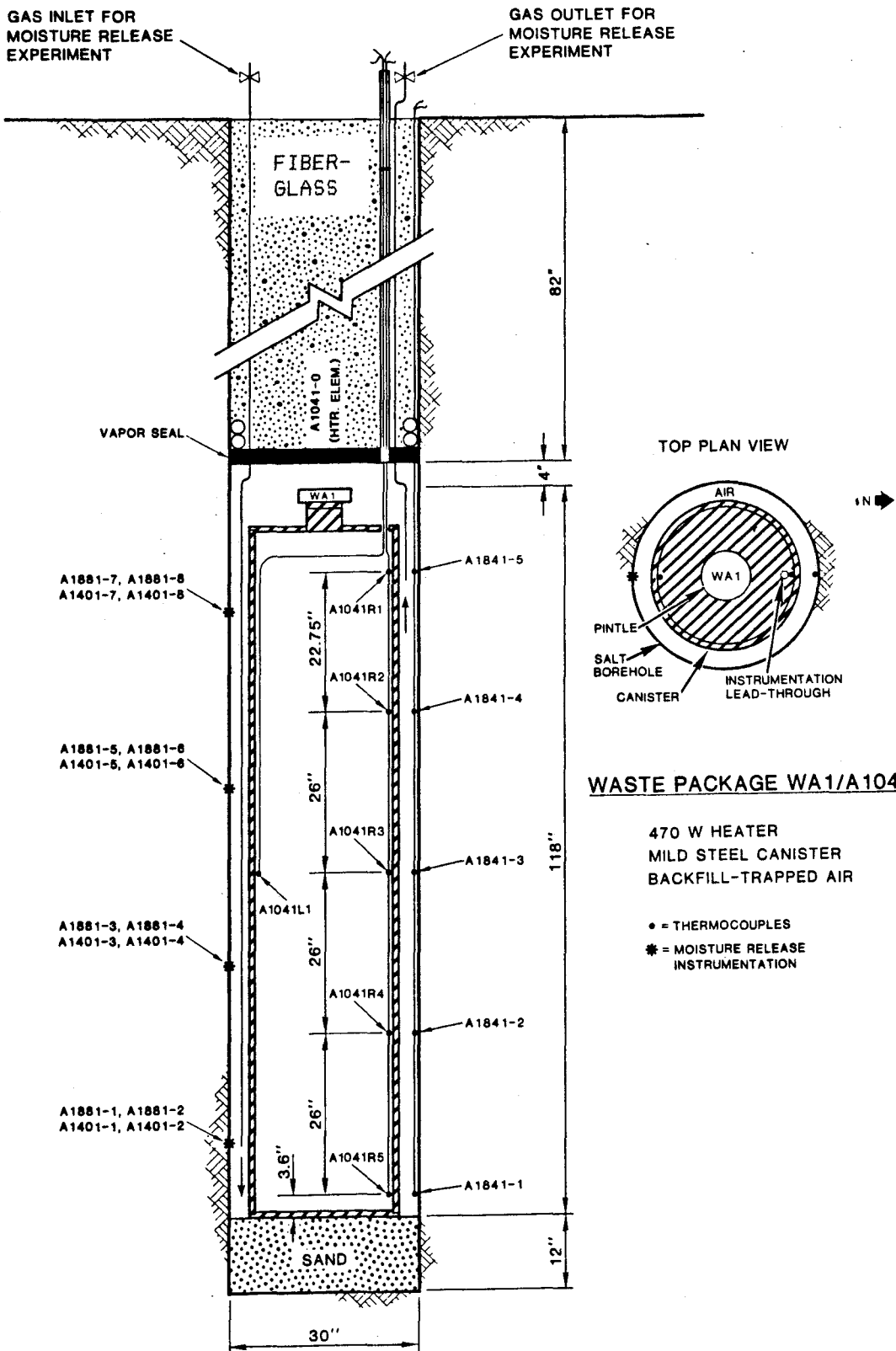


Figure 4: Instrumentation and waste package emplacement WA1.

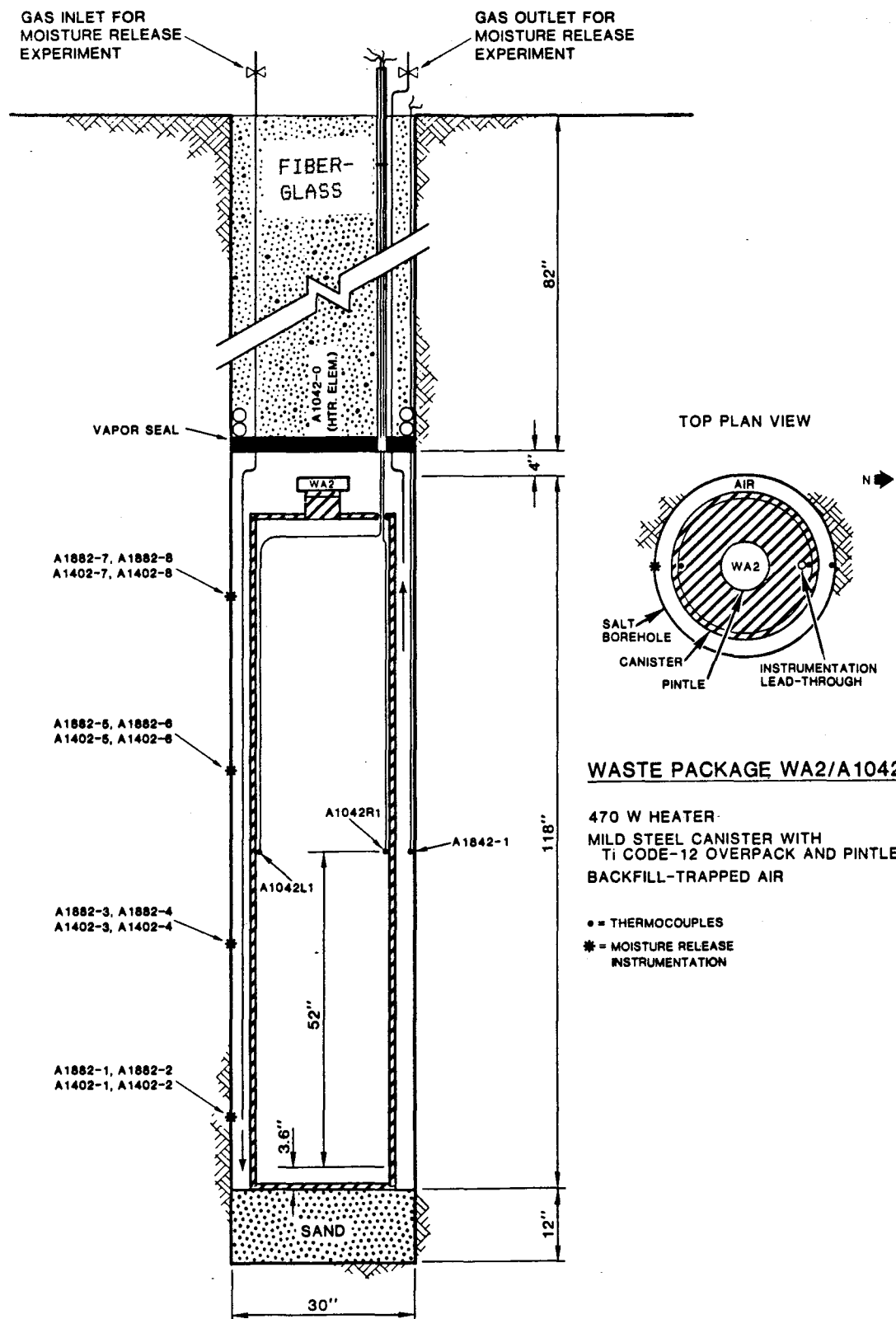


Figure 5: Instrumentation and waste package emplacement WA2.

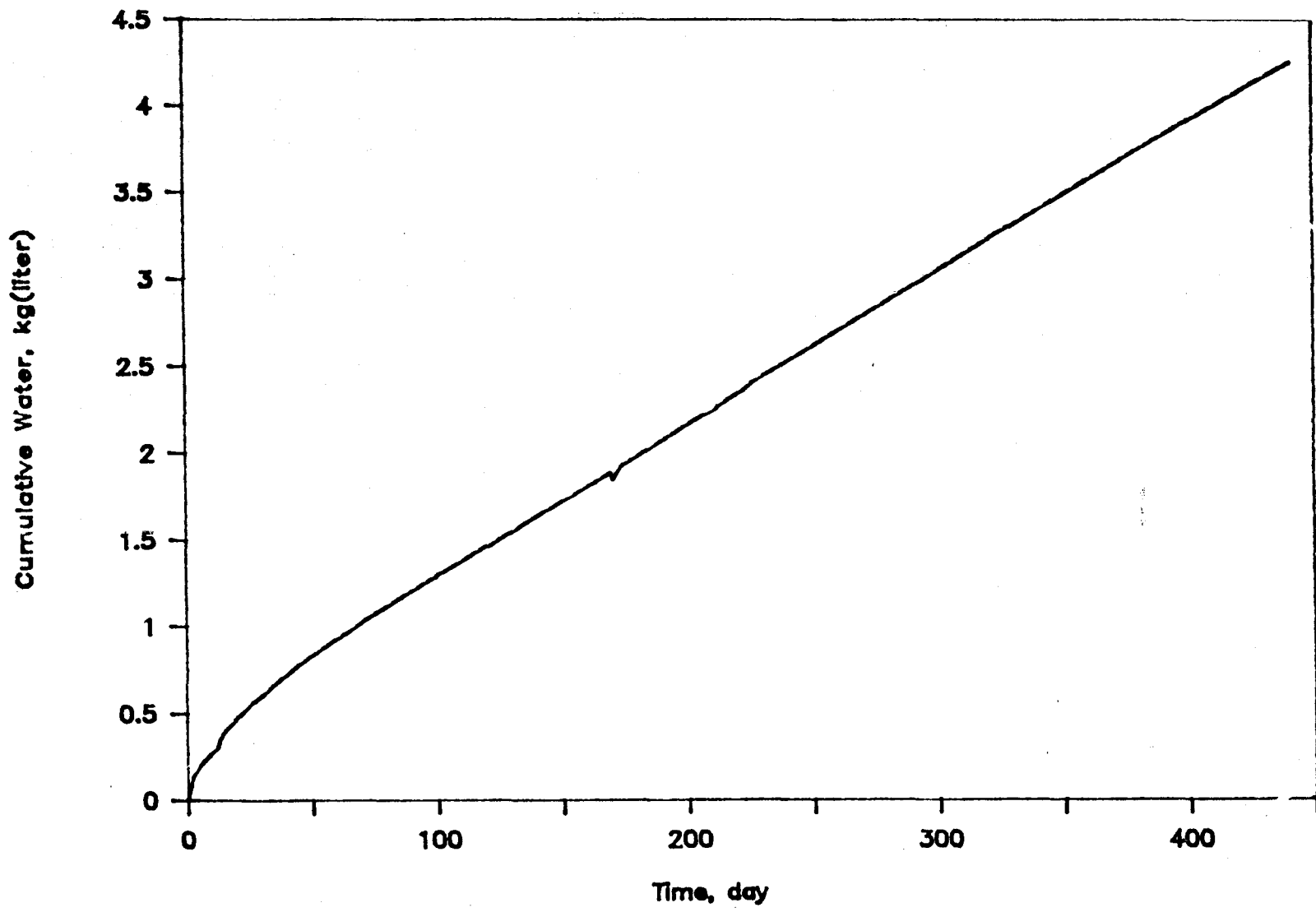


Figure 6: Measured cumulative water *vs.* time, borehole A1041.

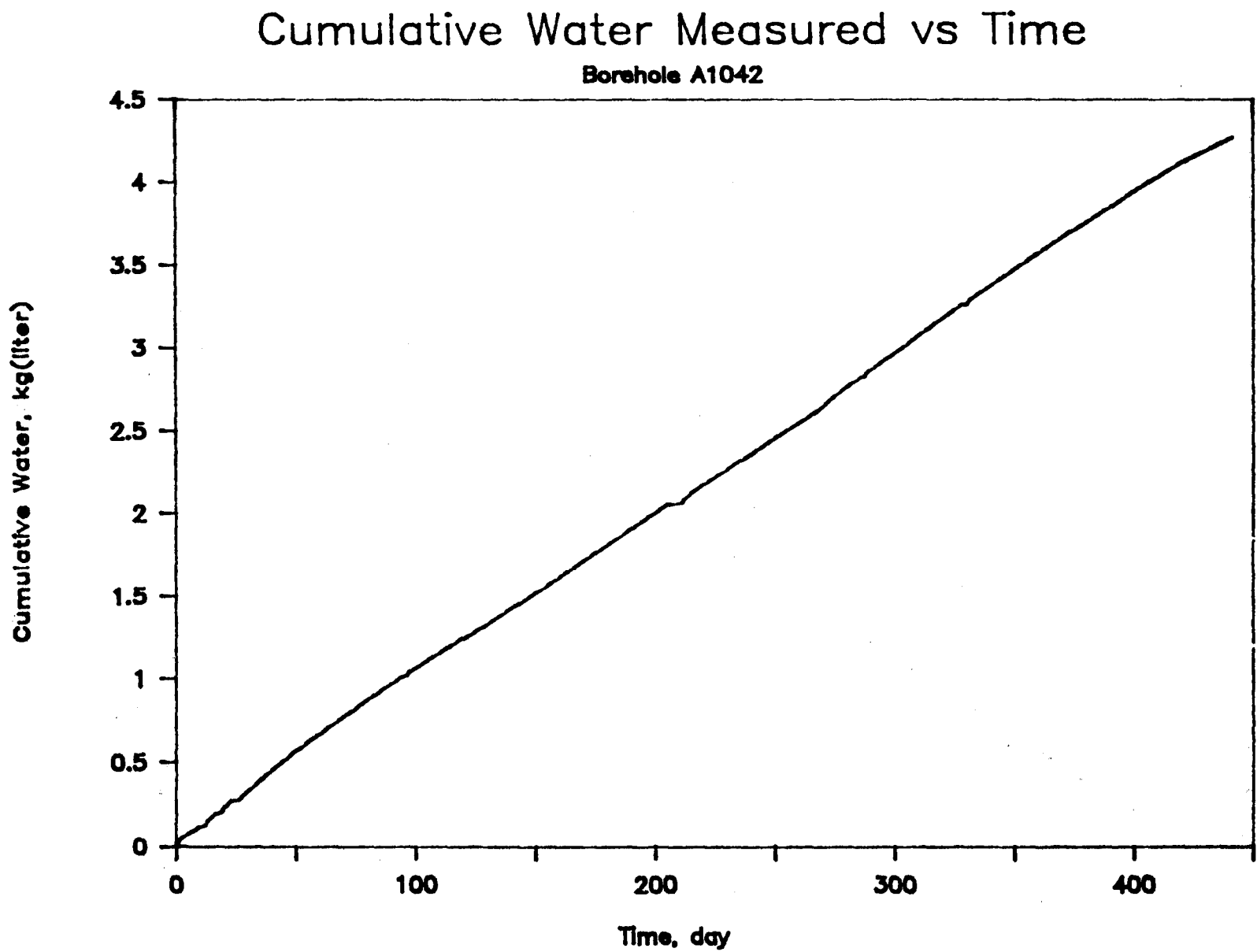


Figure 7: Measured cumulative water *vs.* time, borehole A1042.

Measured Water Inflow Rate vs Time

Borehole A1041

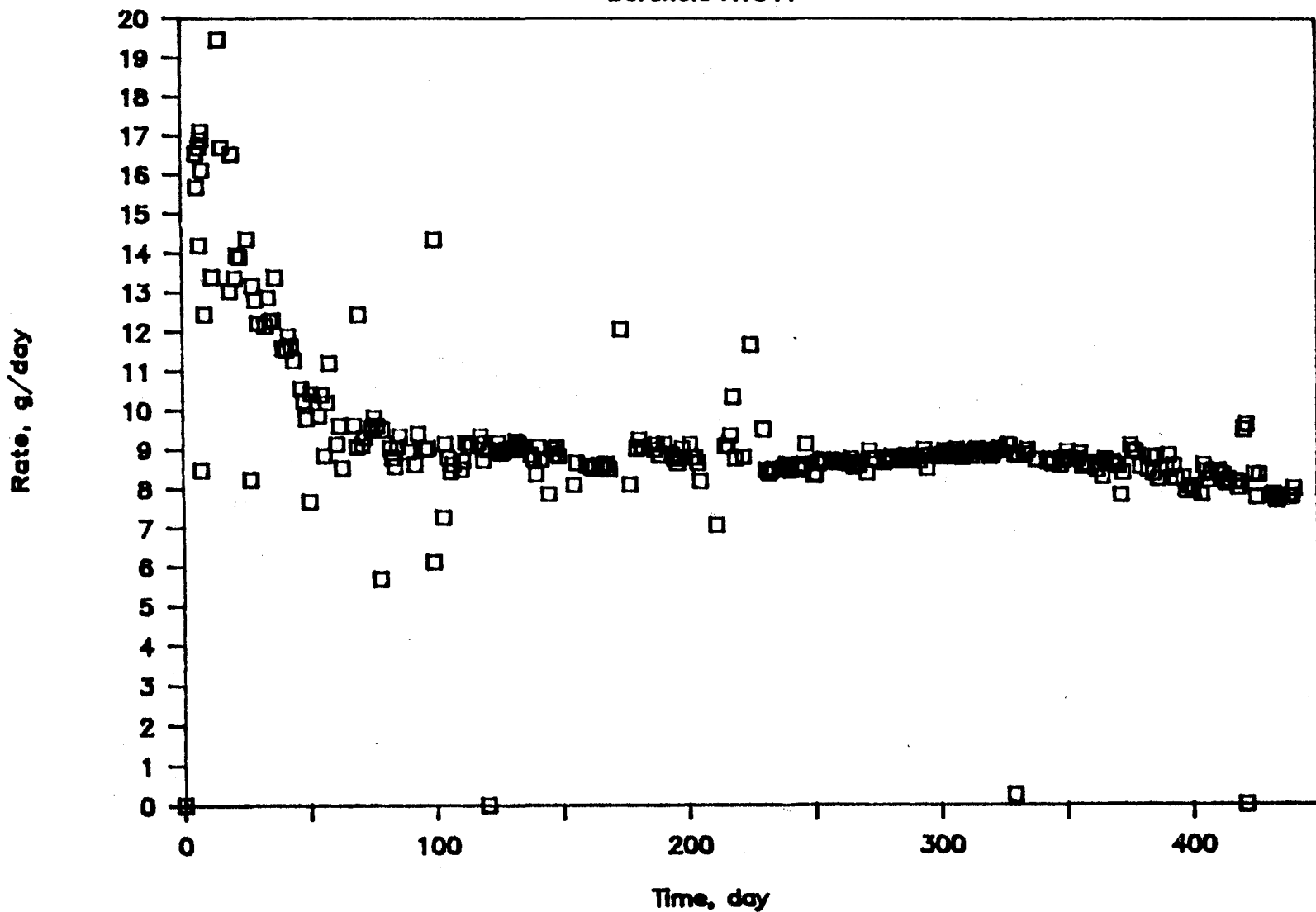


Figure 8: Measured water inflow rate *vs.* time, borehole A1041.

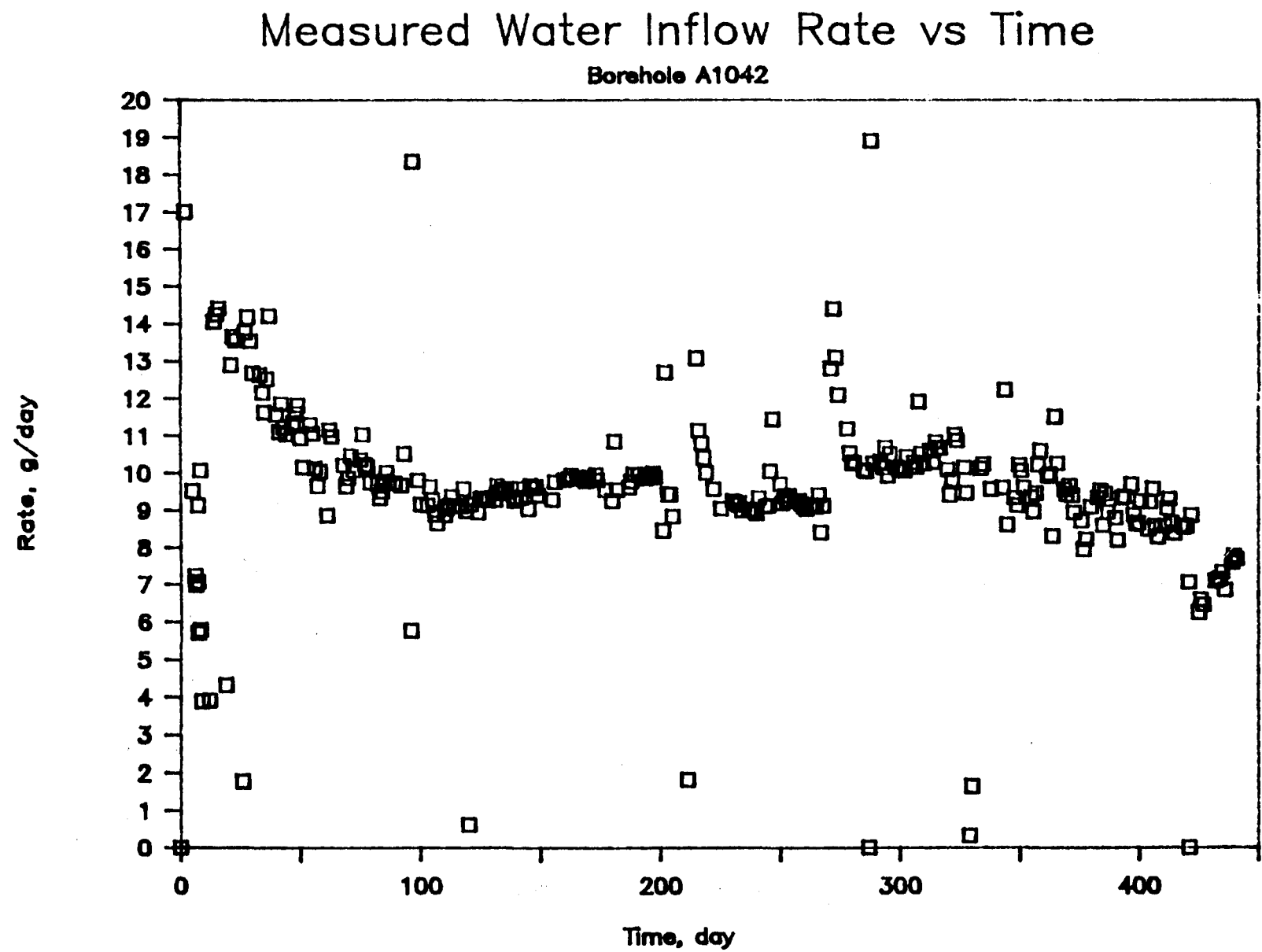


Figure 9: Measured water inflow rate *vs.* time, borehole A1042.

Borehole A1041 Wall Temperature

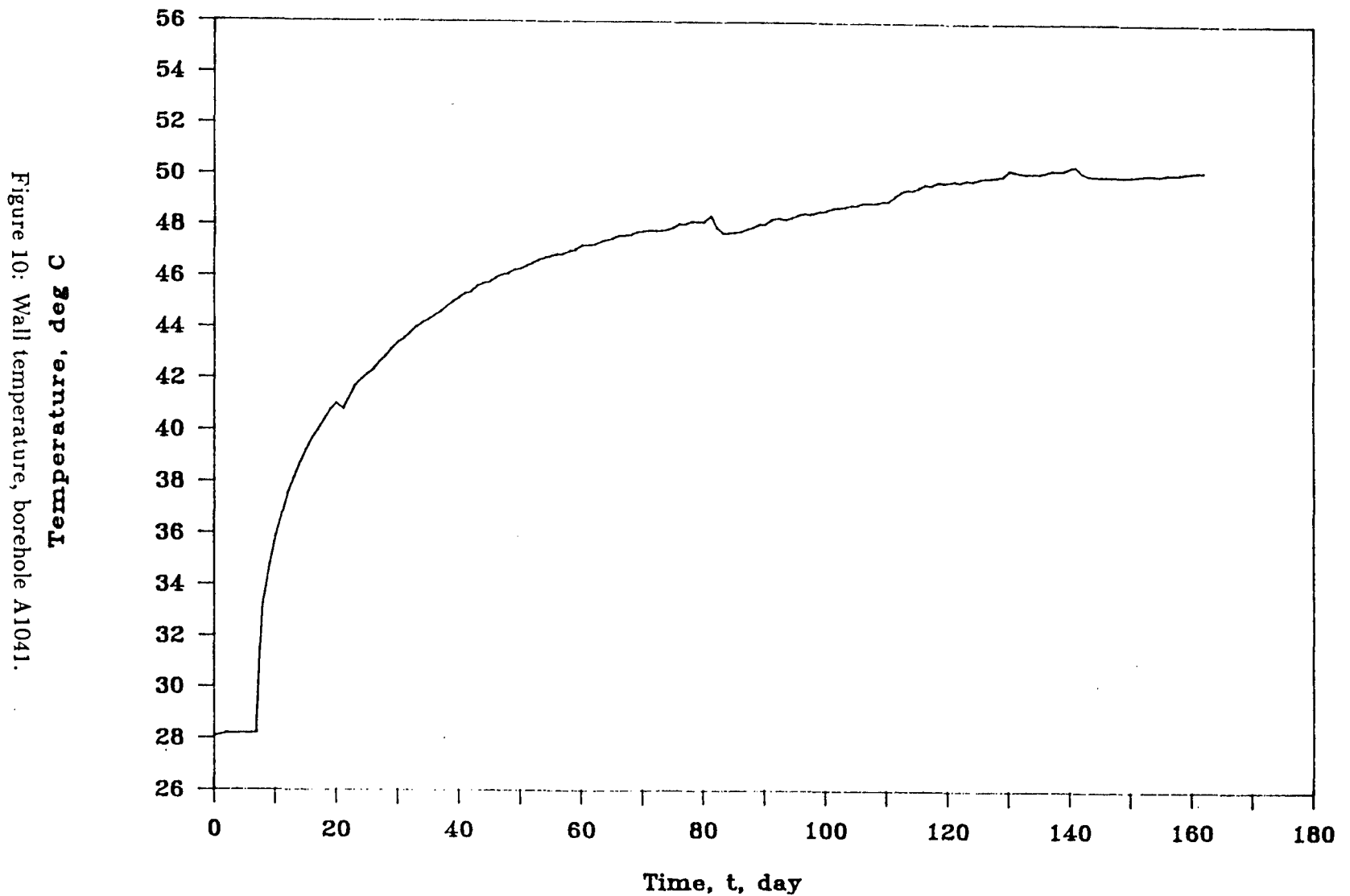


Figure 10: Wall temperature, borehole A1041.

Borehole A1042 Wall Temperature

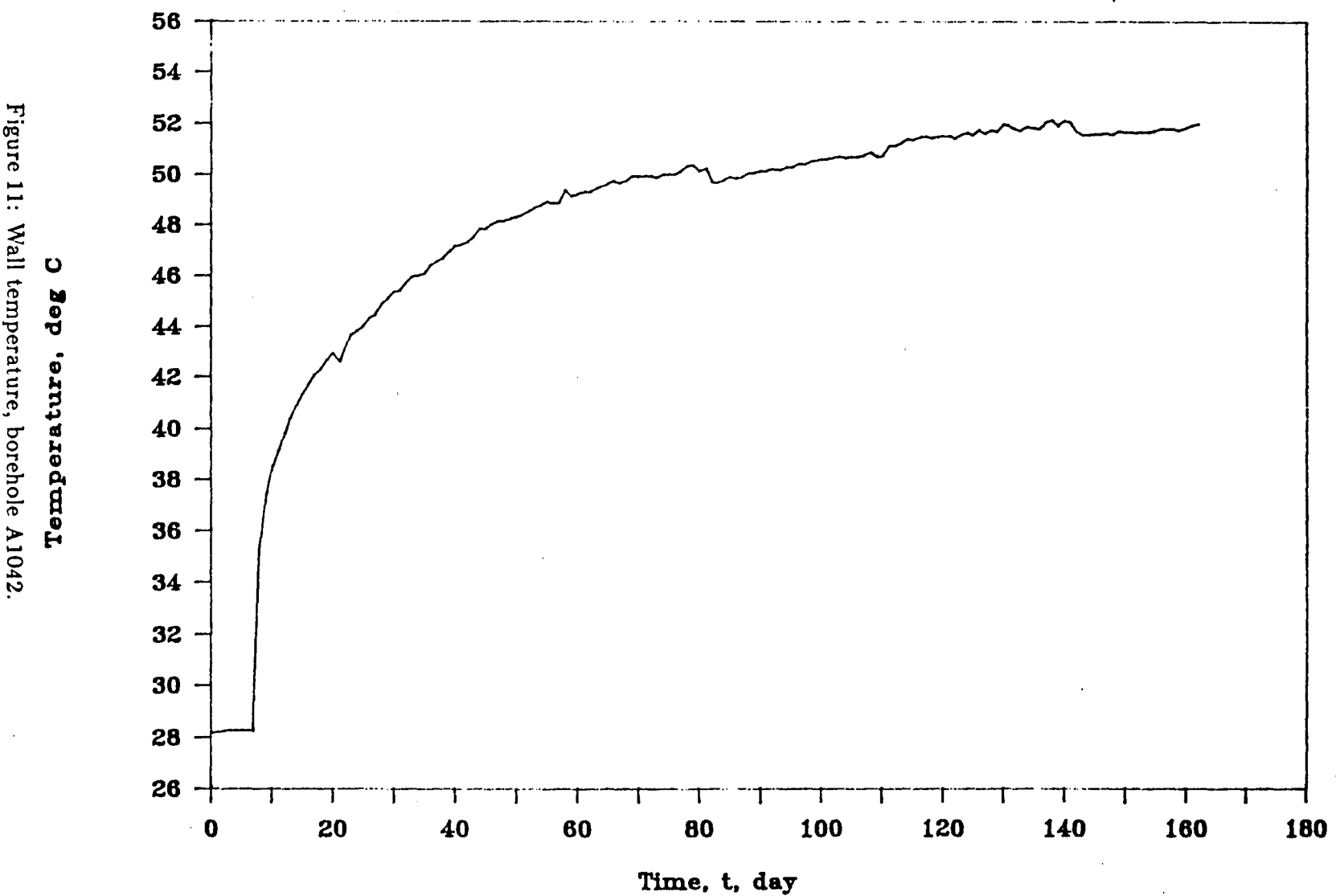


Figure 11: Wall temperature, borehole A1042.

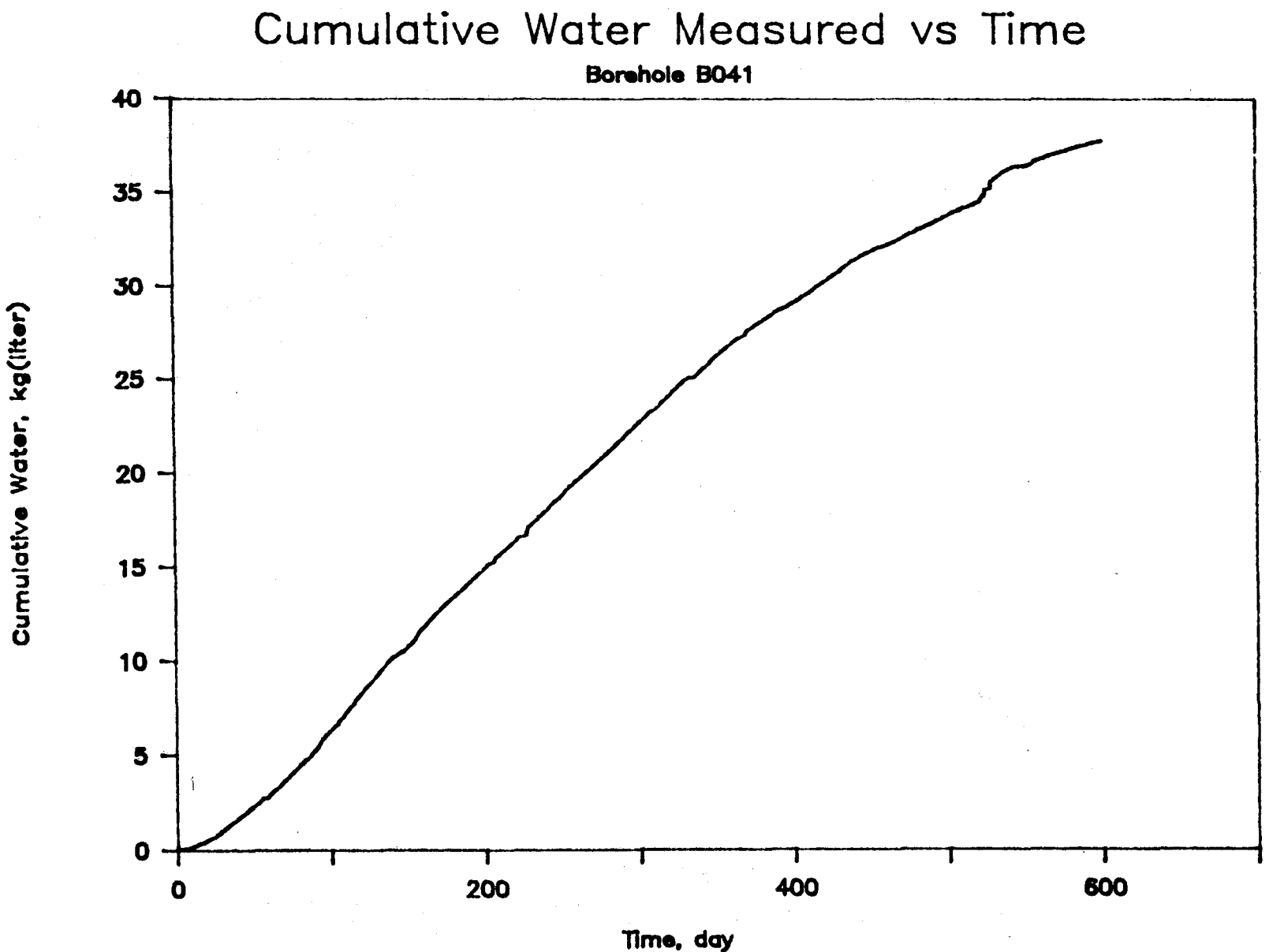


Figure 12: Measured cumulative water *vs.* time, borehole B041.

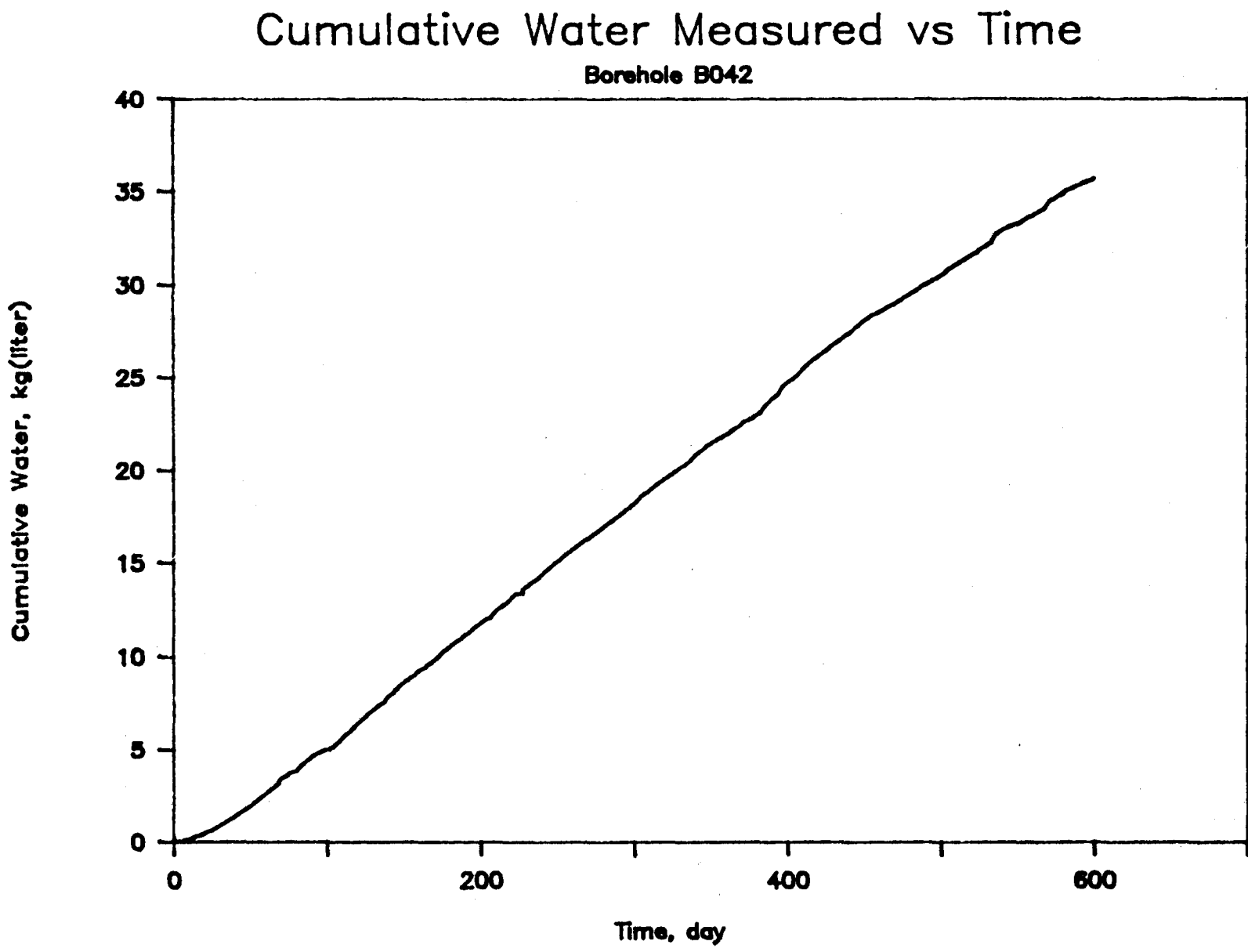


Figure 13: Measured cumulative water *vs.* time, borehole B042.

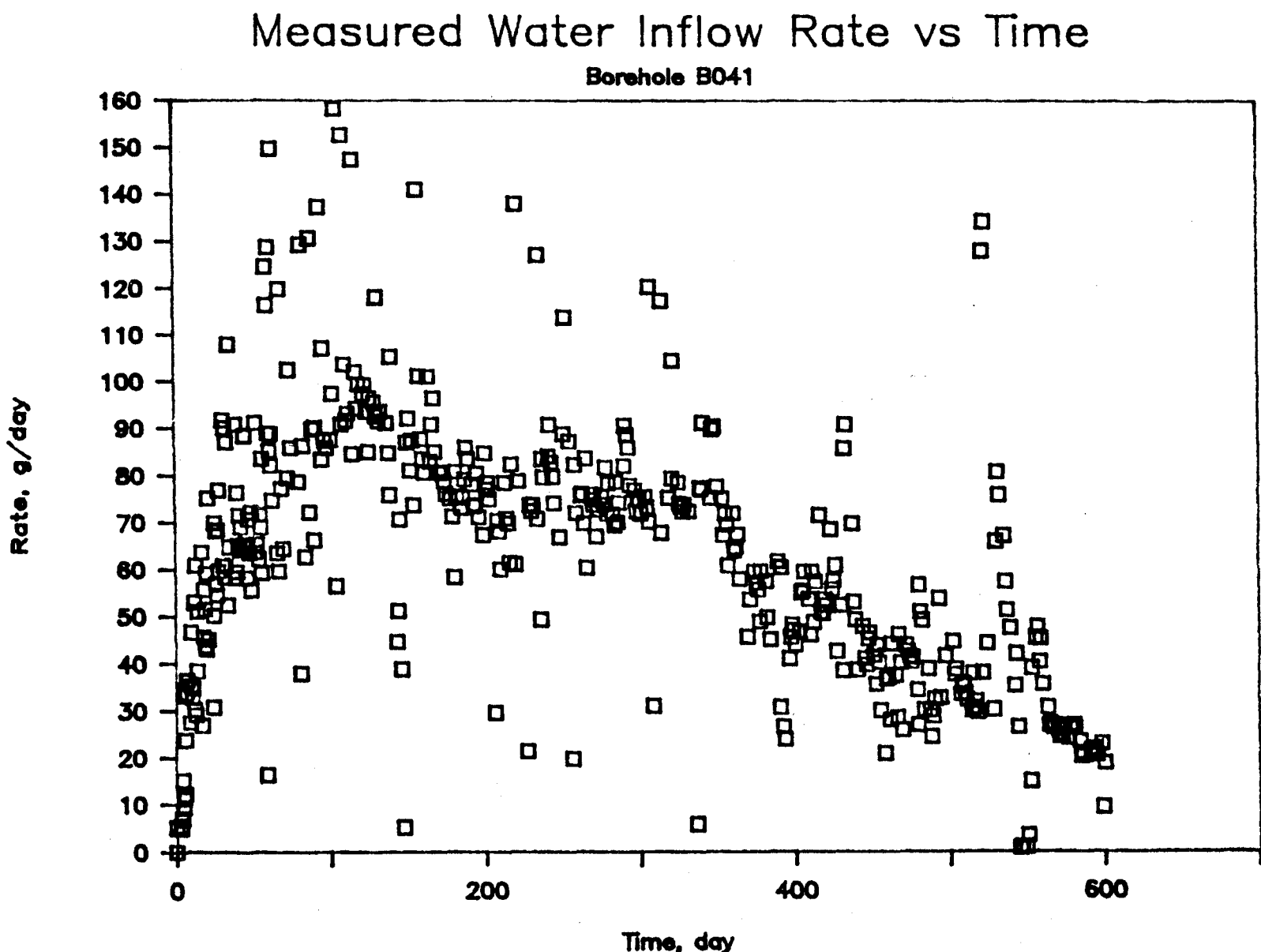


Figure 14: Measured water inflow rate *vs.* time, borehole B041.

Measured Water Inflow Rate vs Time

Borehole B042

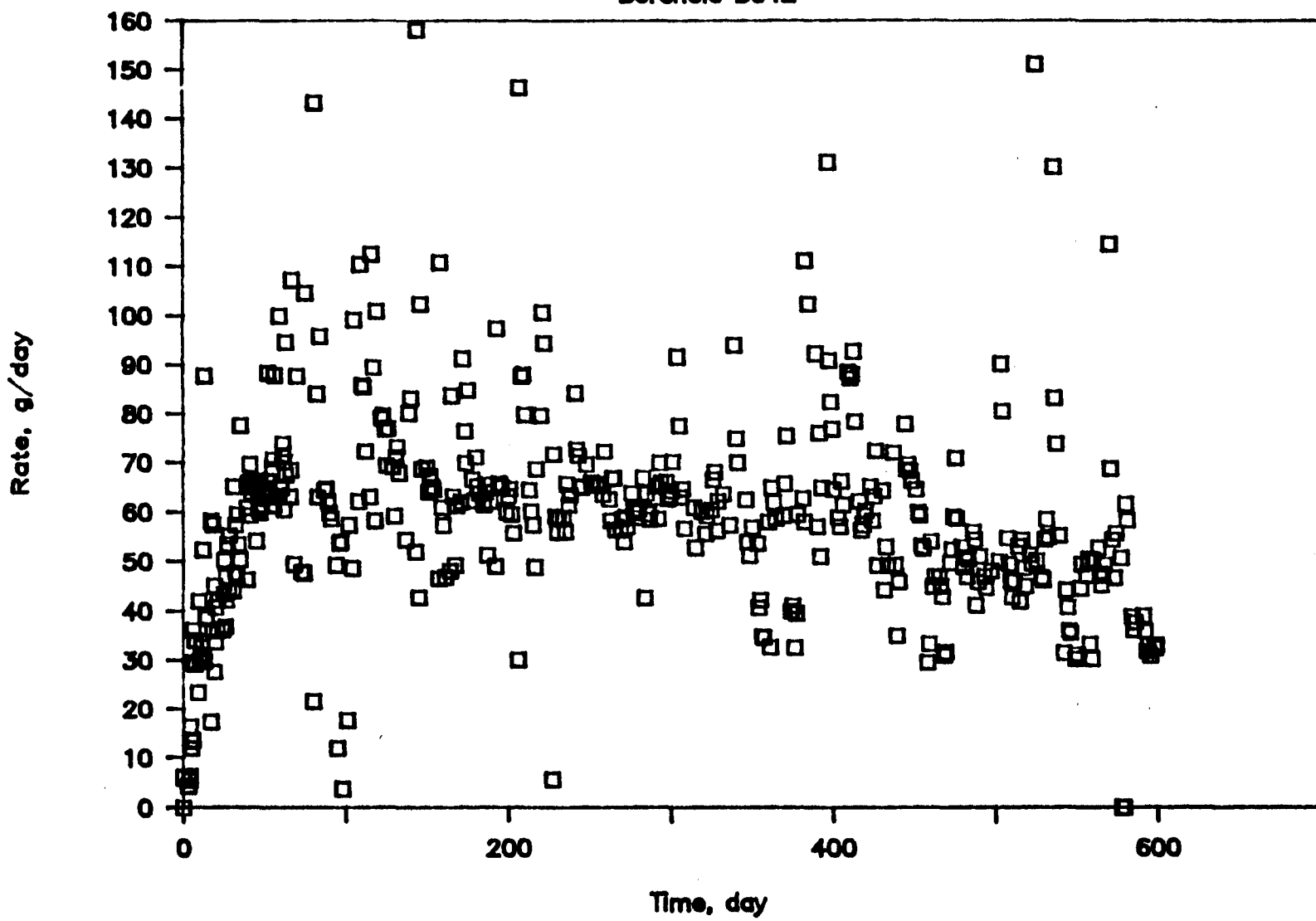


Figure 15: Measured water inflow rate vs. time, borehole B042.

Borehole B041 Wall Temperature

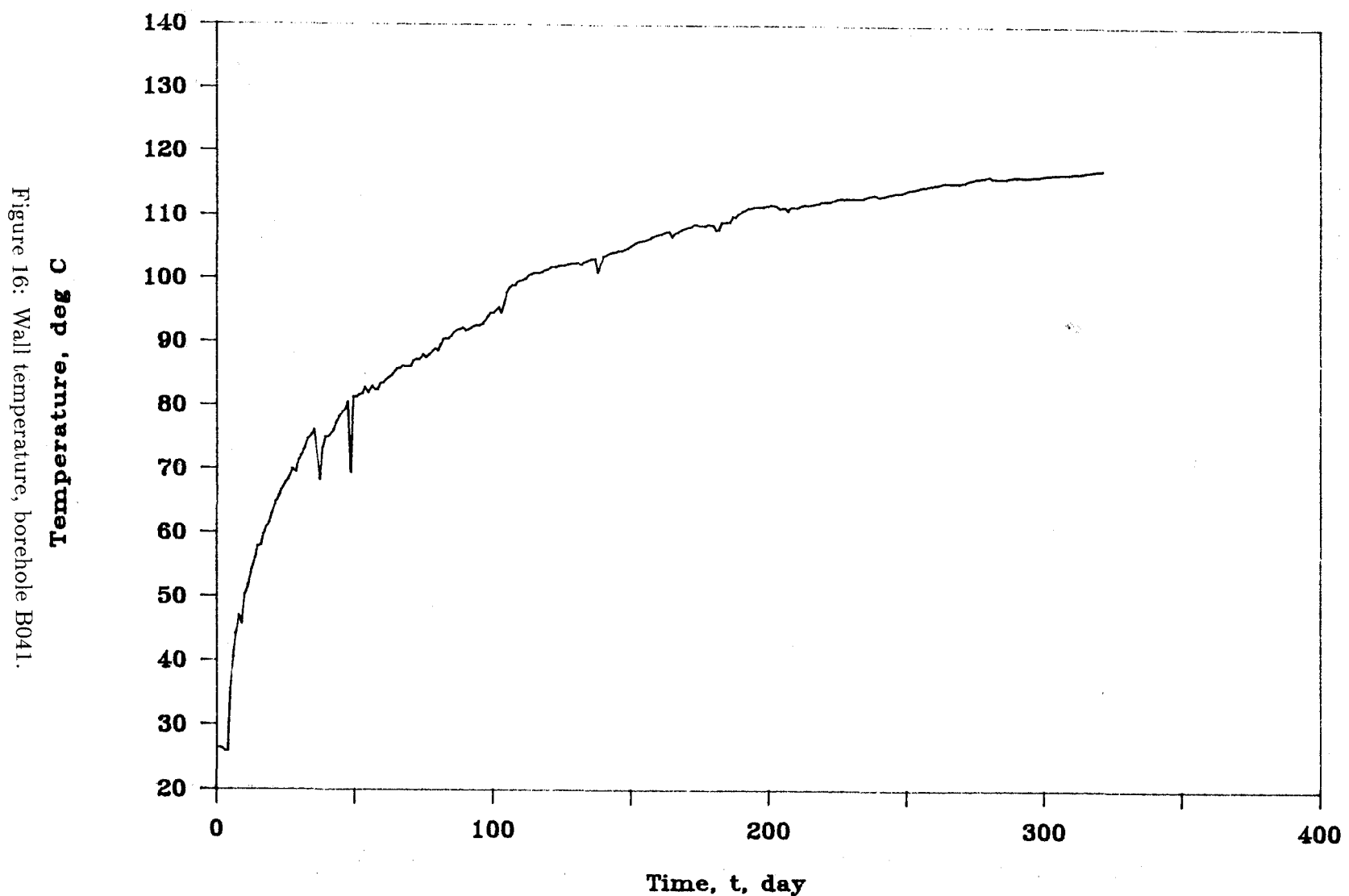


Figure 16: Wall temperature, borehole B041.

Borehole B042 Wall Temperature

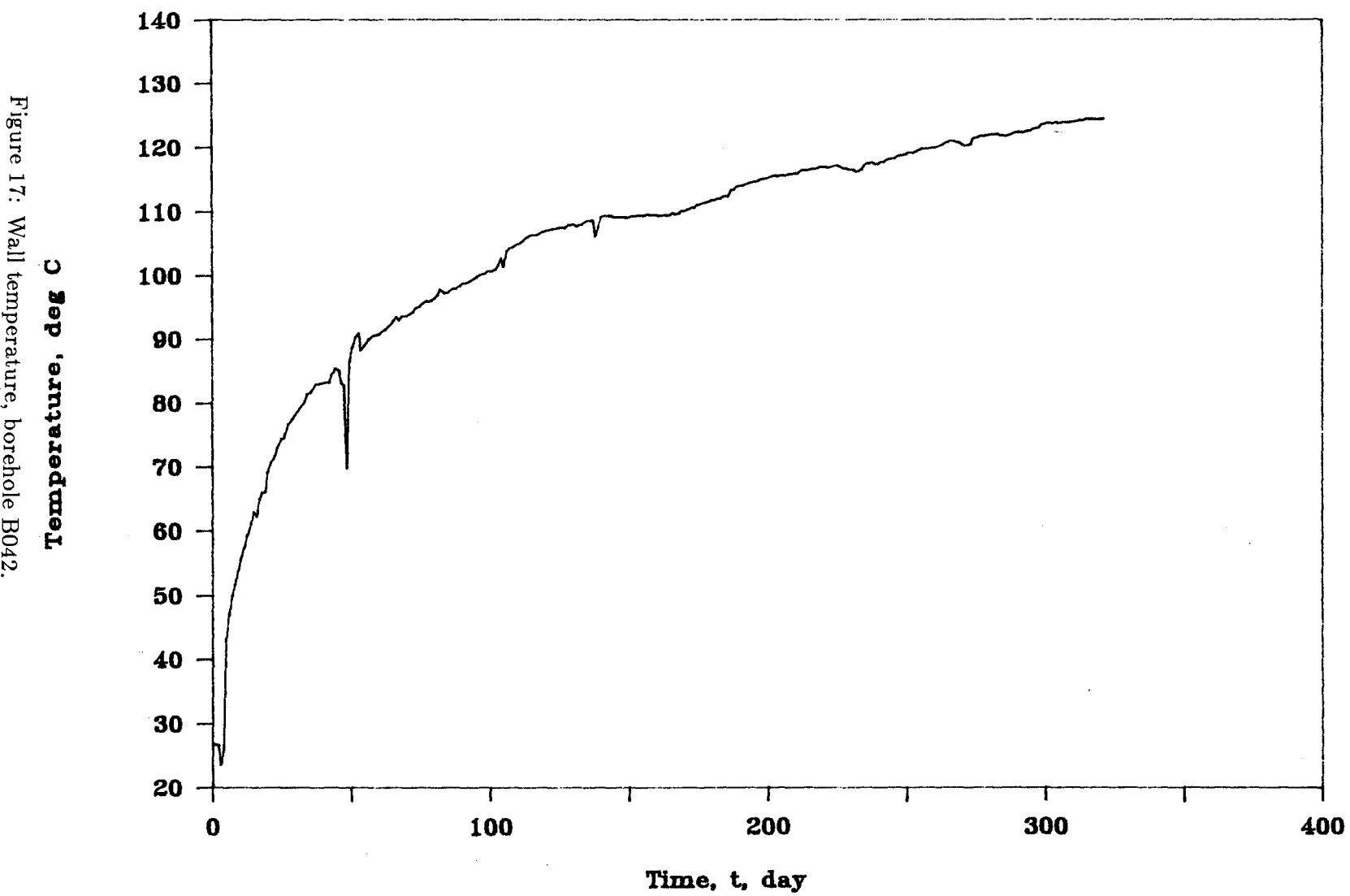


Figure 17: Wall temperature, borehole B042.

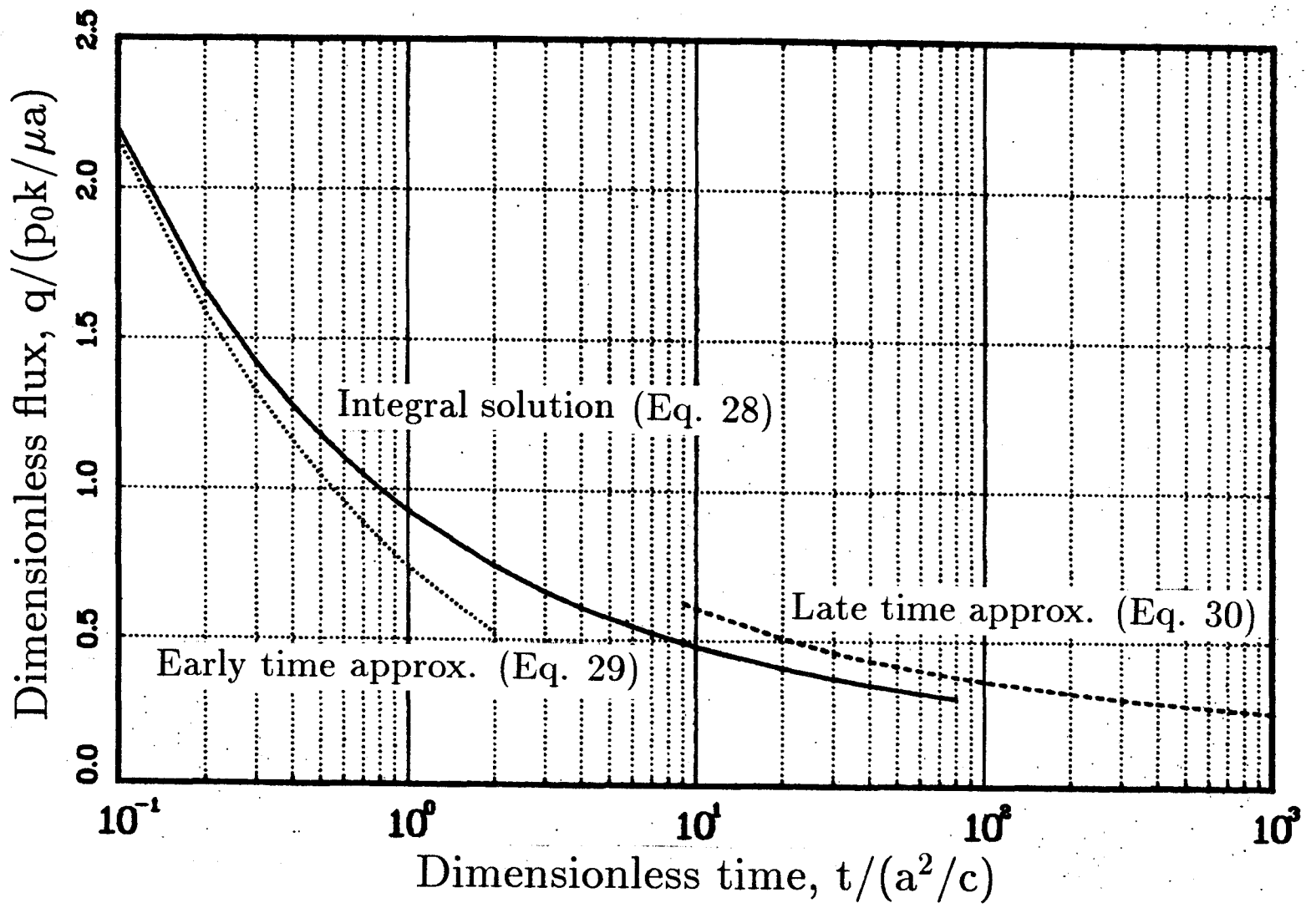


Figure 18: Dimensionless flux *vs.* time for flow to a circular tunnel.

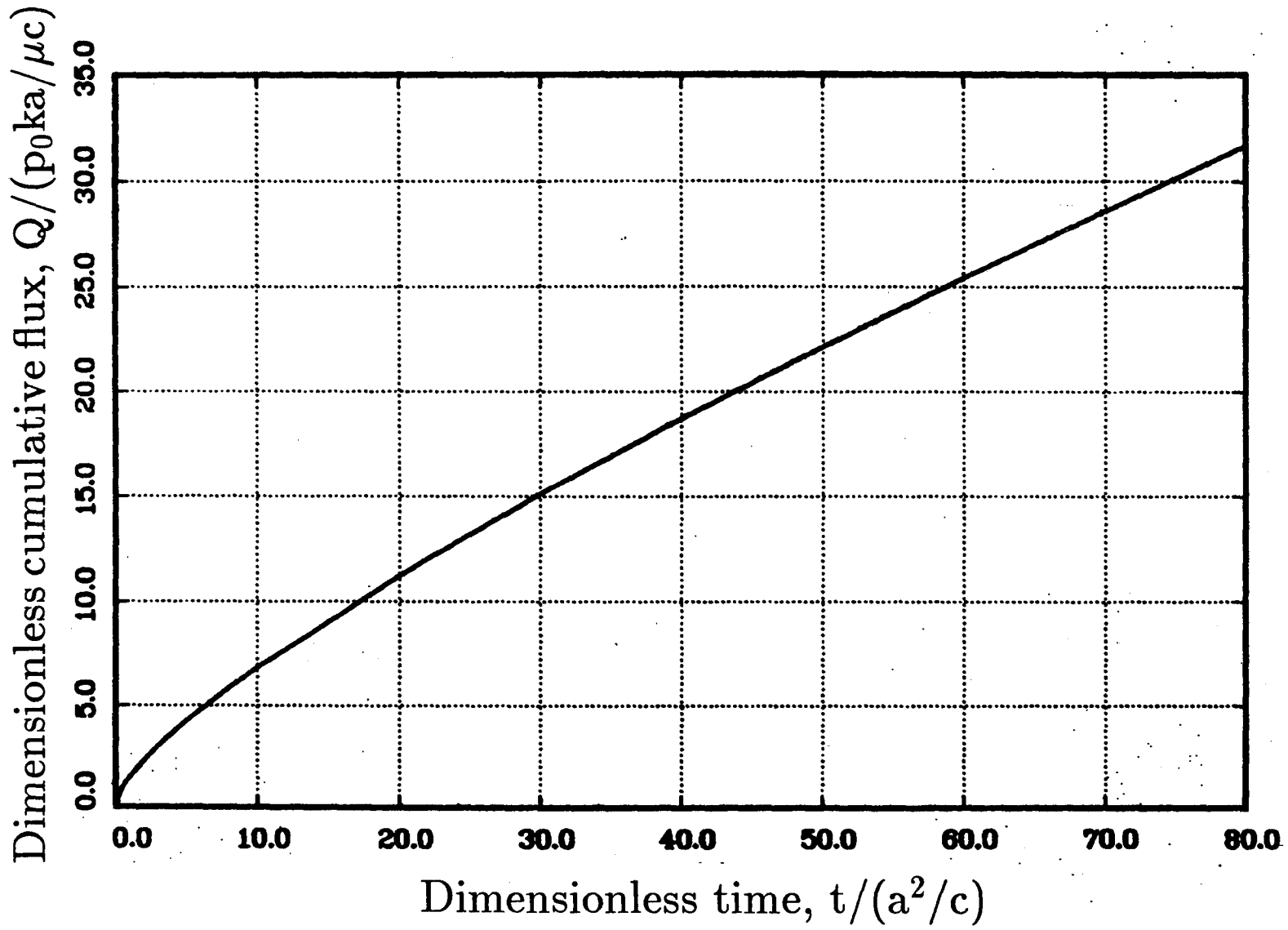


Figure 19: Dimensionless cumulative flux *vs.* time for flow to a circular tunnel.

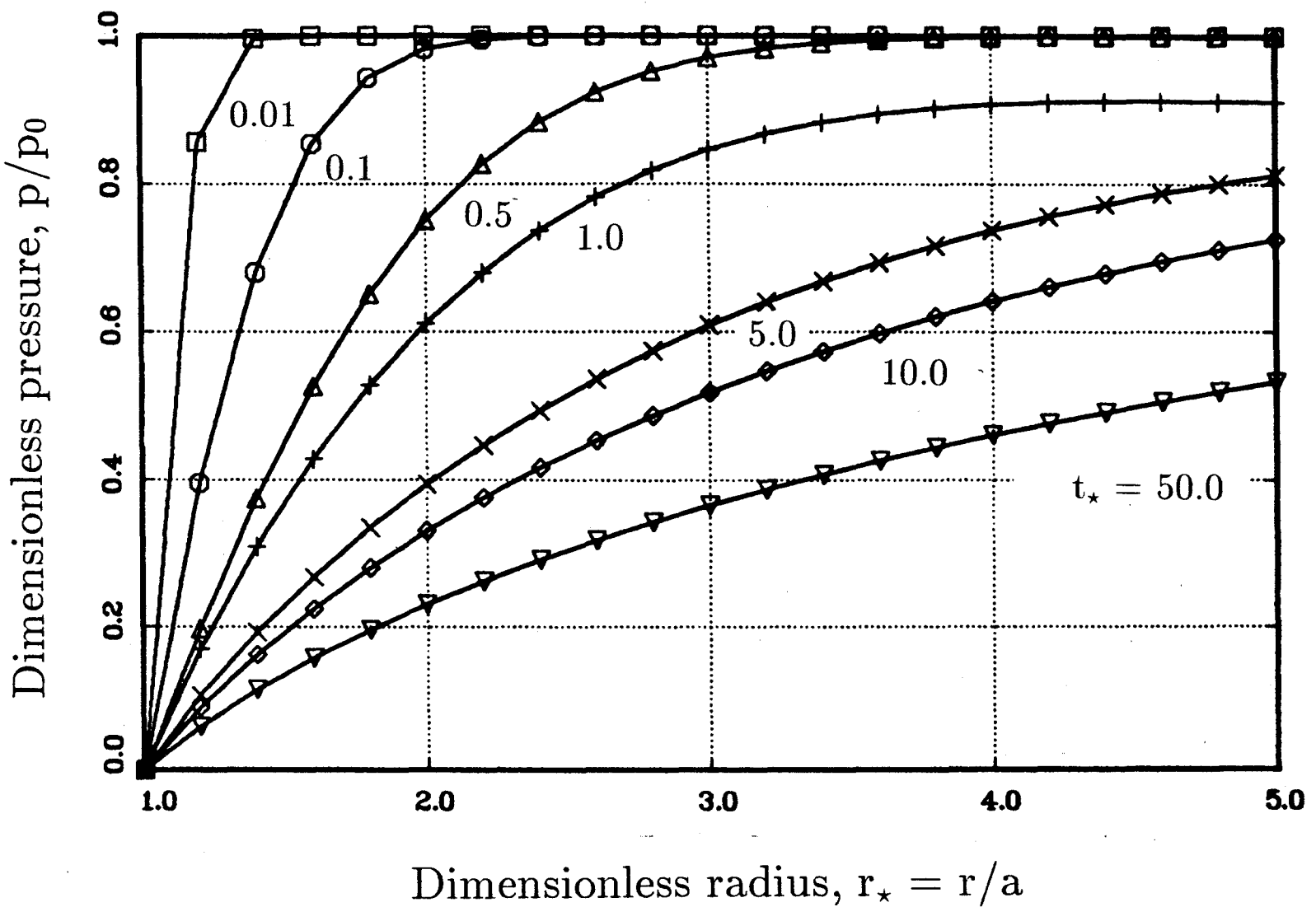
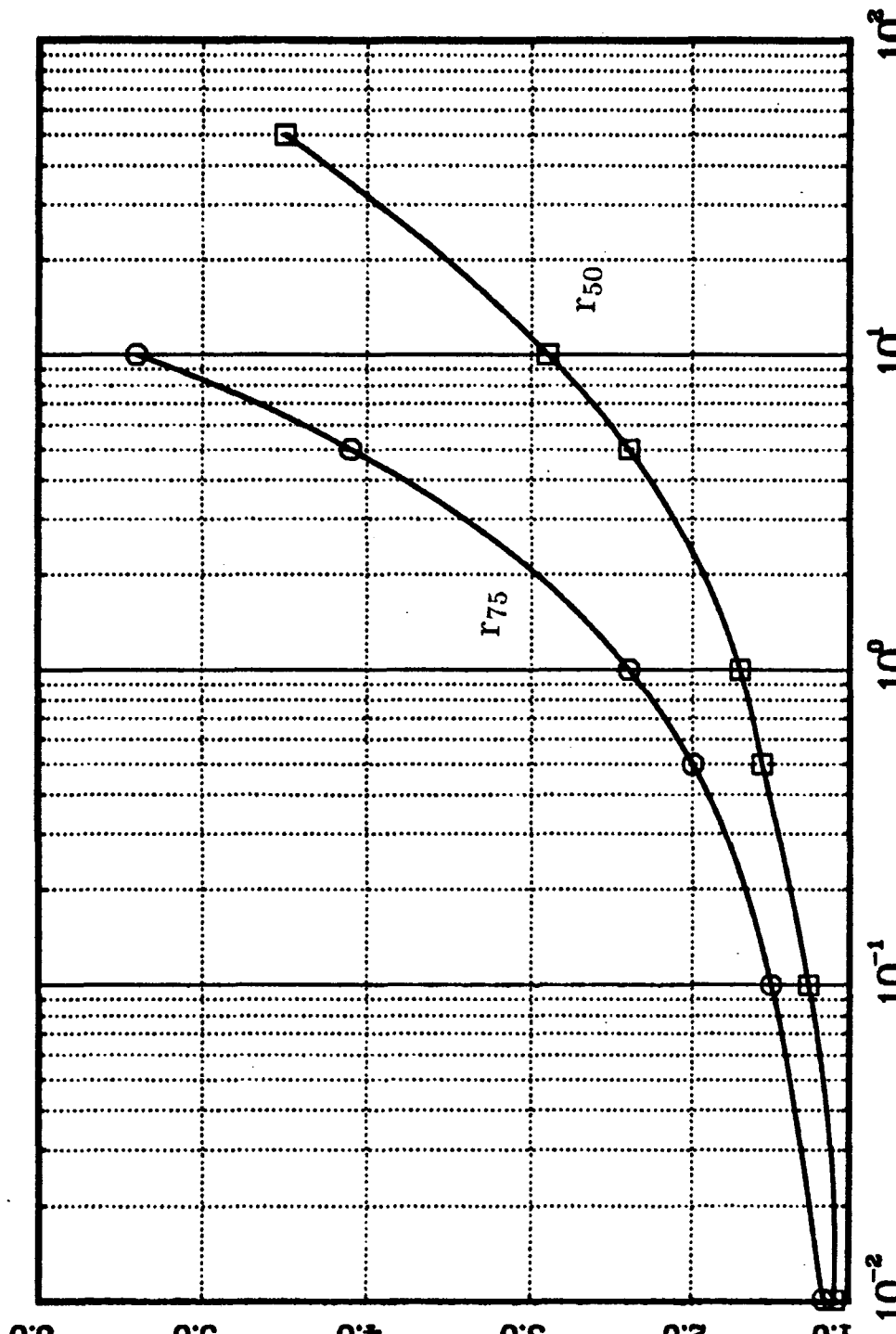


Figure 20: Dimensionless pore pressure profiles due to flow to a tunnel.



Dimensionless radius, $r^* = r/a$

Dimensionless time, $t^* = t/(a^2/c)$

Figure 21: Dimensionless radius and time at which pore pressure has relaxed to 50% and 75% of its intial value.

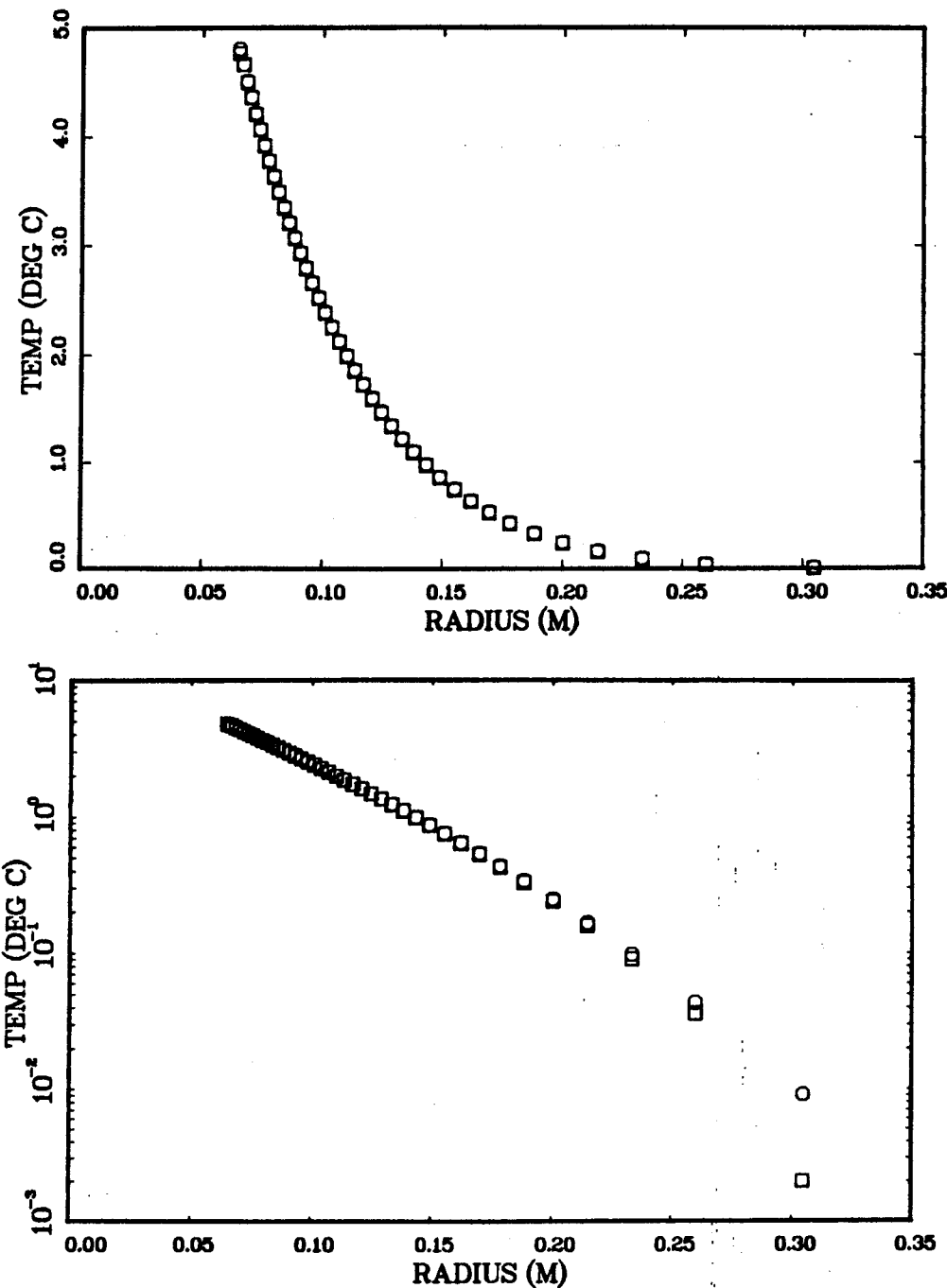


Figure 22: Comparison of exact analytical solution (squares) of (34)–(37) and numerical solution (circles) of (45)–(48). Test problem is for $a = 0.065$ m, $q_0 = 610$ W/m², $K = 6.6$ W/m/K, $\kappa = 3.5 \times 10^{-6}$ m²/s, $\zeta = 1.0$. Profile is for $t = 1200$ s. Semilog plot reveals error at large r .

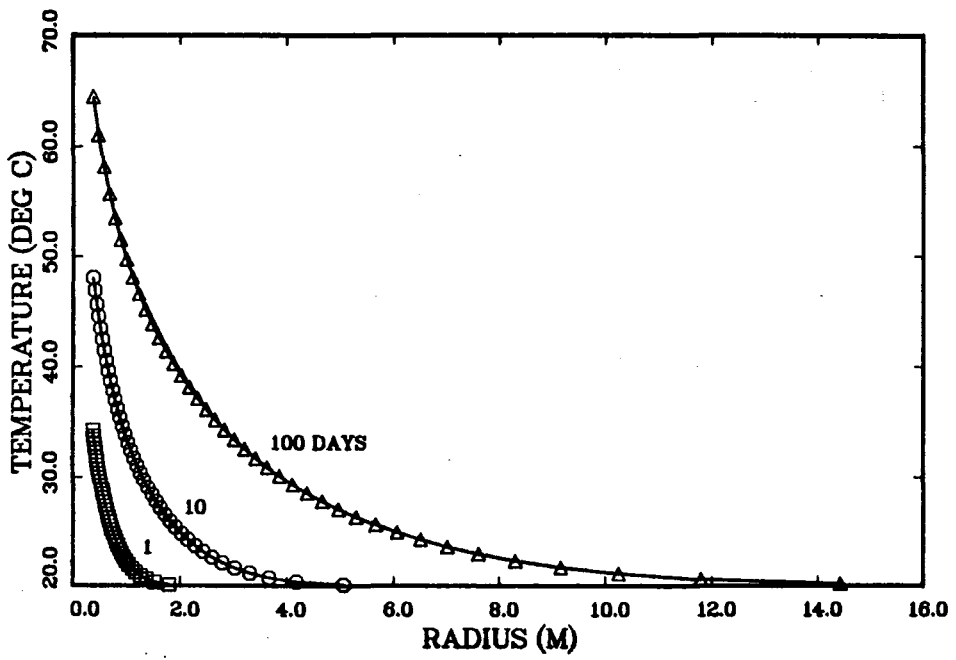


Figure 23: Temperature profiles at $t = 1, 10$, and 100 days. Note the stretching of the nodal spacing with increasing distance from the hole (the last node is at $r \rightarrow \infty$).

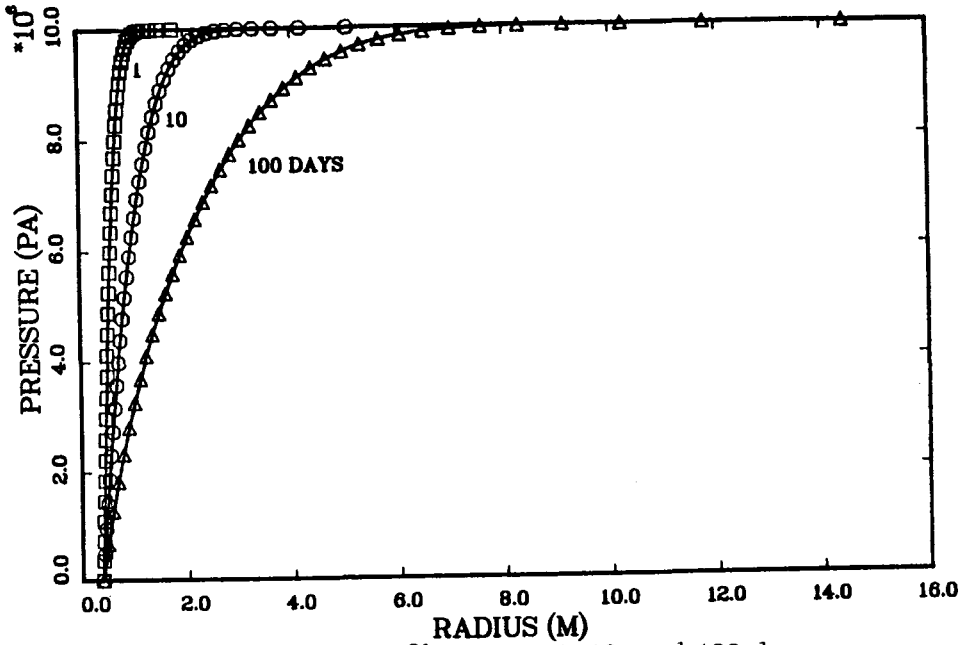


Figure 24: Pressure profiles at $t = 1, 10$, and 100 days.

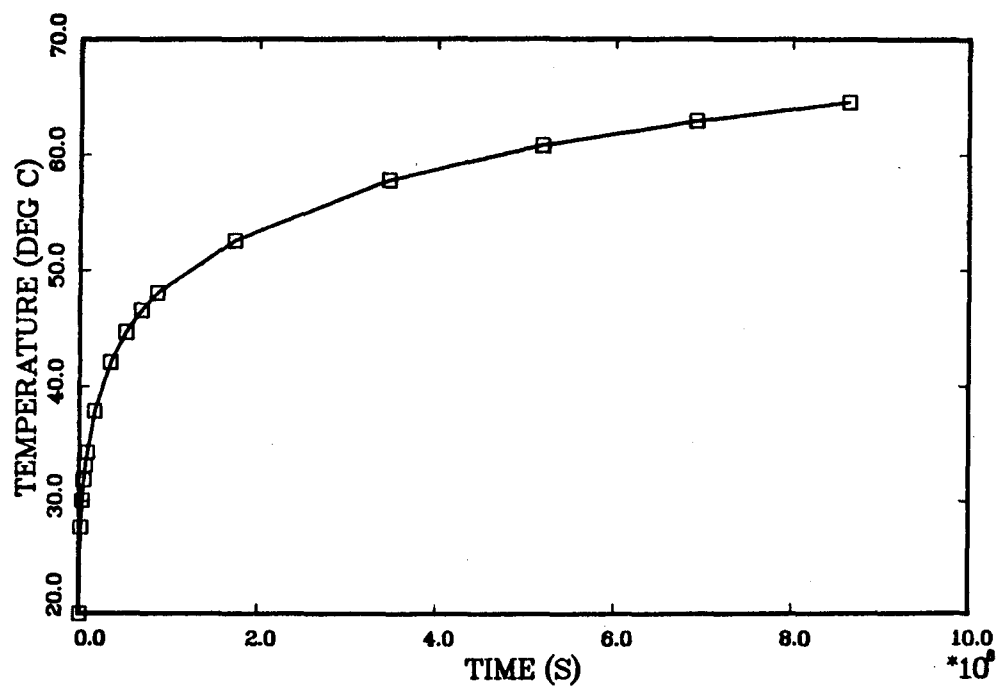


Figure 25: Borehole wall temperature rise over 100 days (8.64×10^6 s).

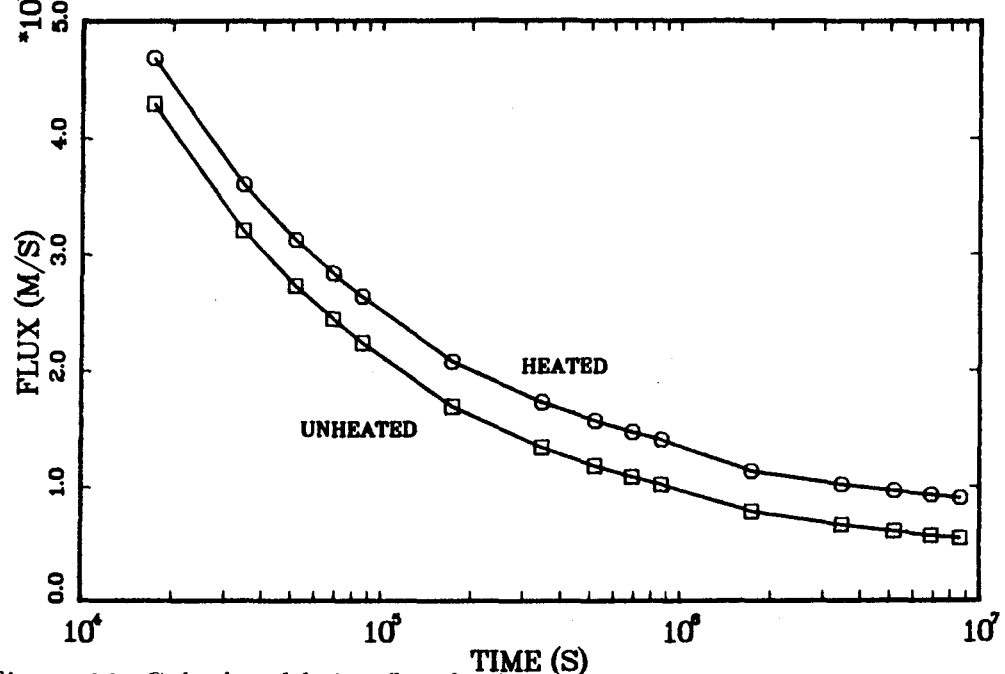


Figure 26: Calculated brine flux for heated and unheated boreholes over 100 days

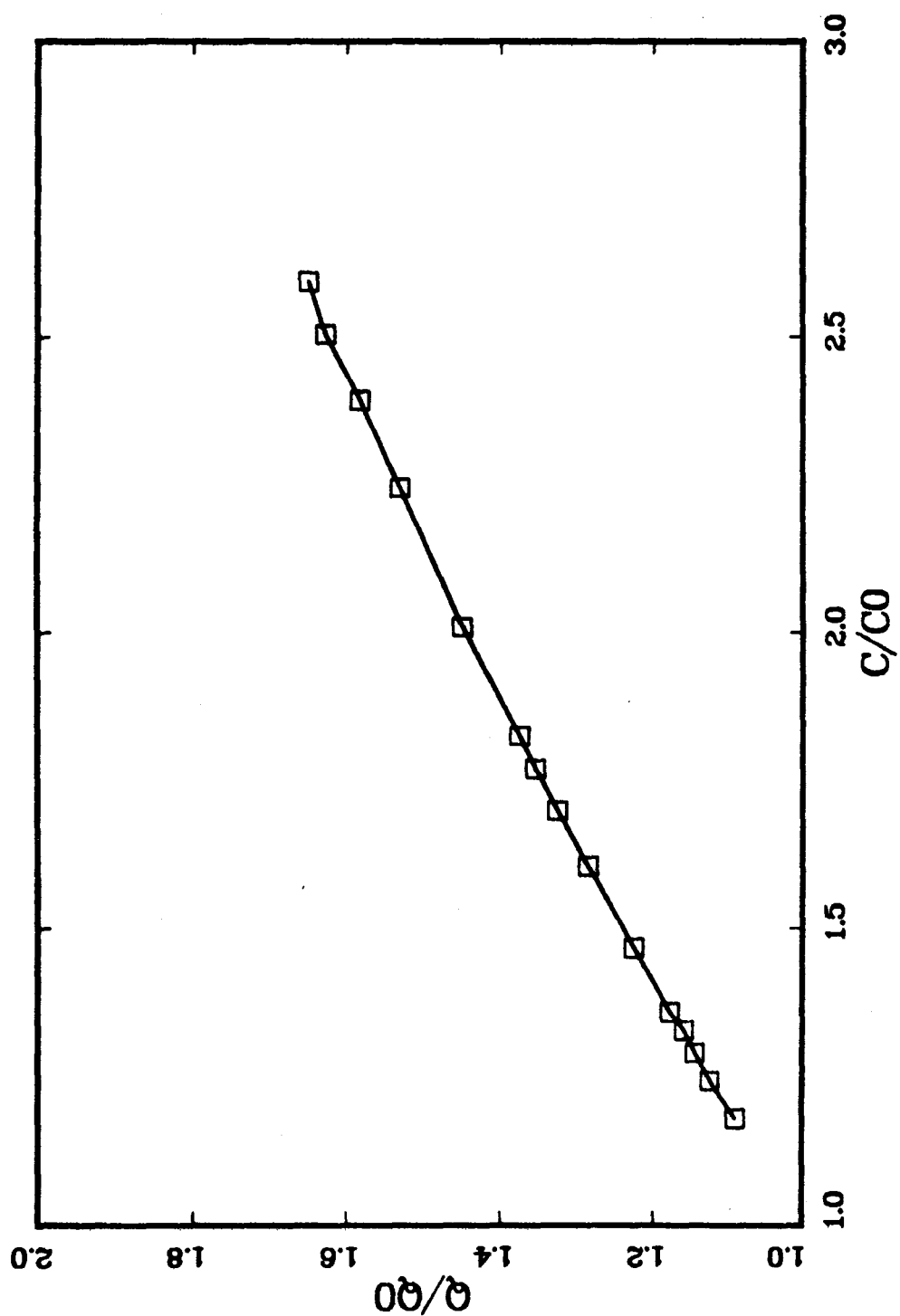


Figure 27: Increase in fluid flux compared to increase in diffusivity, both normalized by values for the isothermal case. Highest relative flux and diffusivity correspond to 100 days.

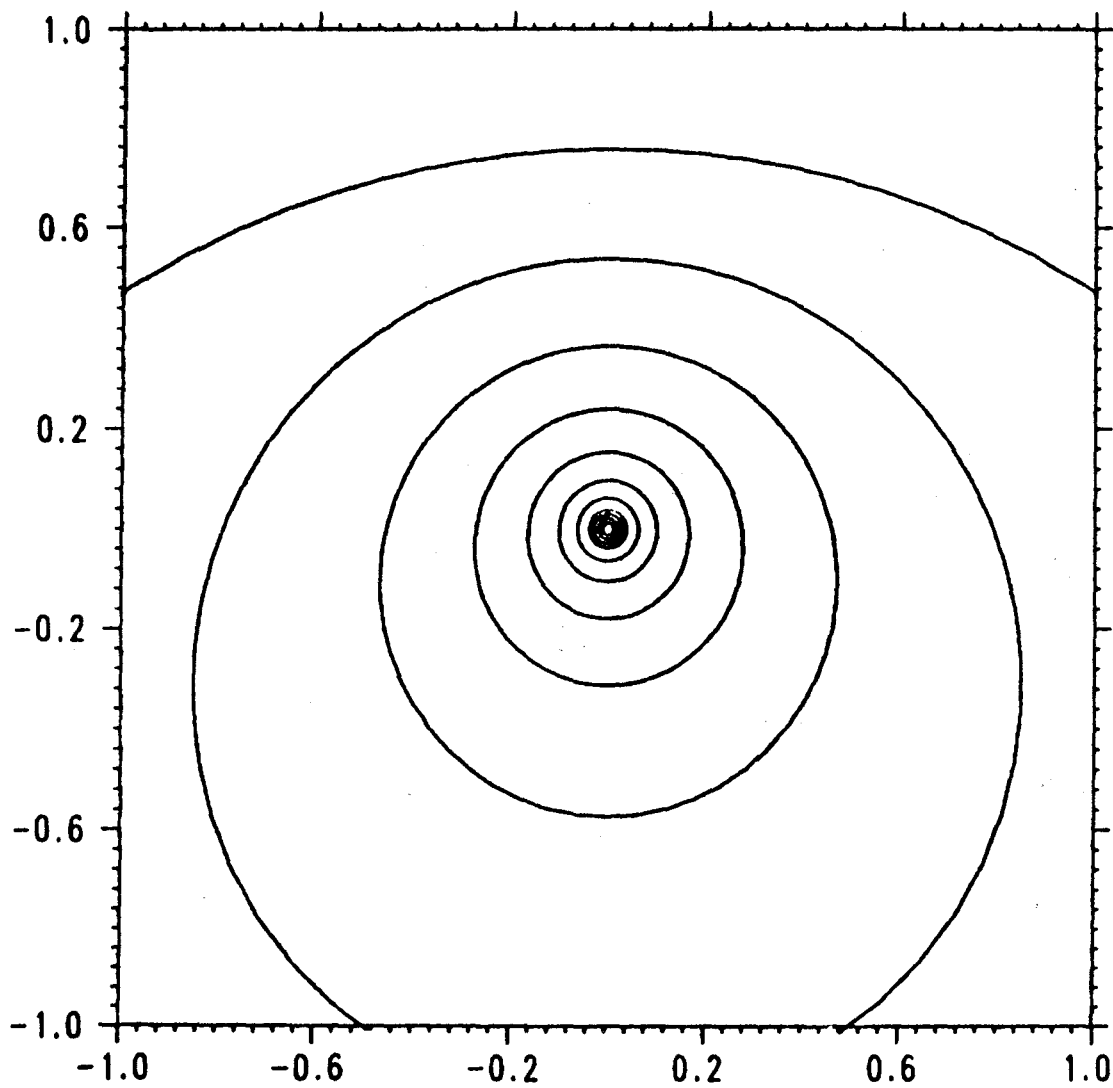


Figure 28: Potential field for flow to a line sink (Eq. 58). Vertical scale is for $z_* + 1$, the dimensionless coordinate centered at the line sink, and scaled by the depth, d . The horizontal scale is also normalized by the depth d . Equipotentials shown are scaled by $Q\mu/2\pi k$; for the sample problem discussed, the equipotentials shown correspond to zero at the free surface, decreasing by increments of approximately 1 MPa, to a value of -11.7 MPa at the tunnel.

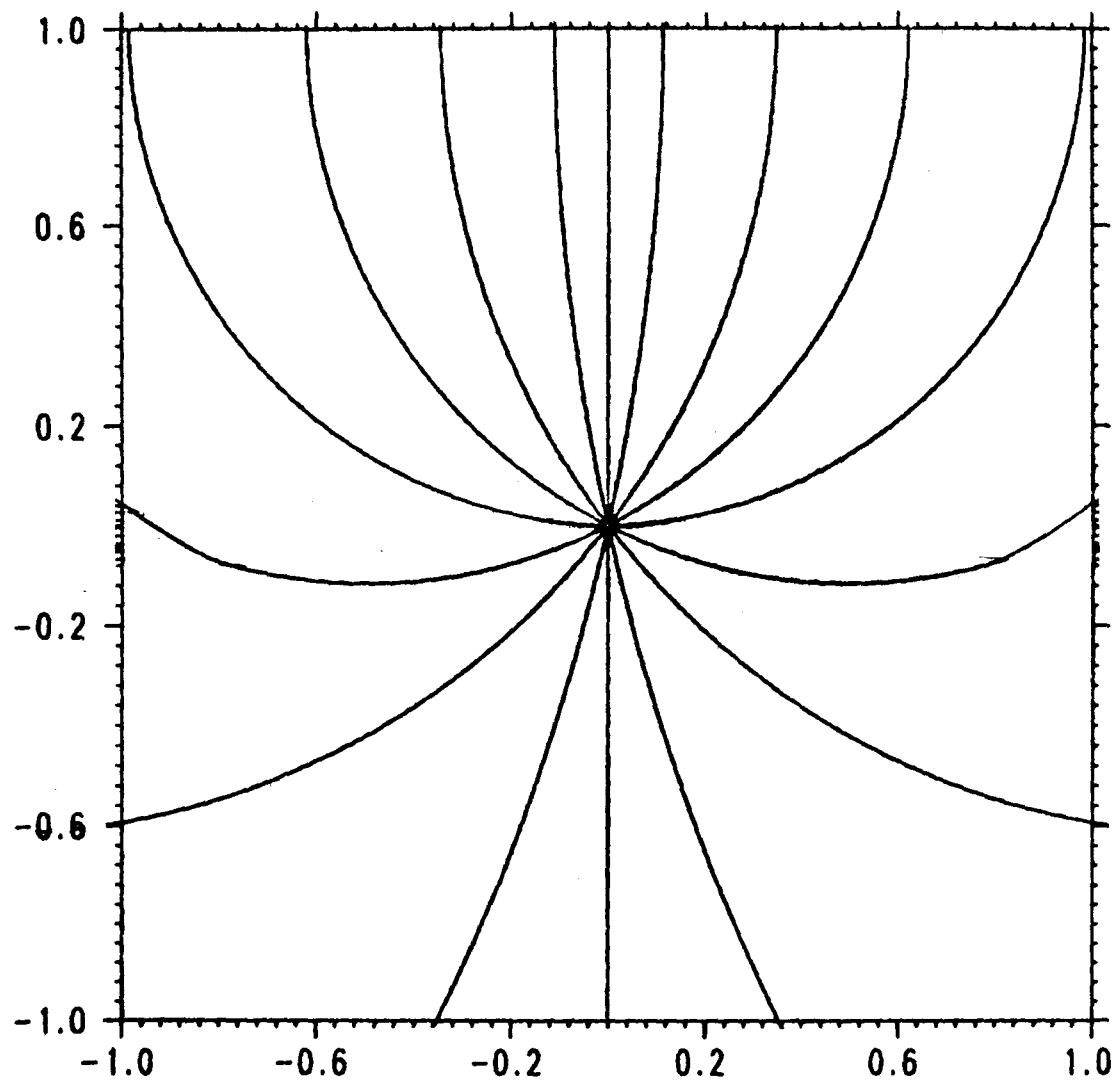


Figure 29: Streamlines corresponding to the potential field shown in Figure 28.

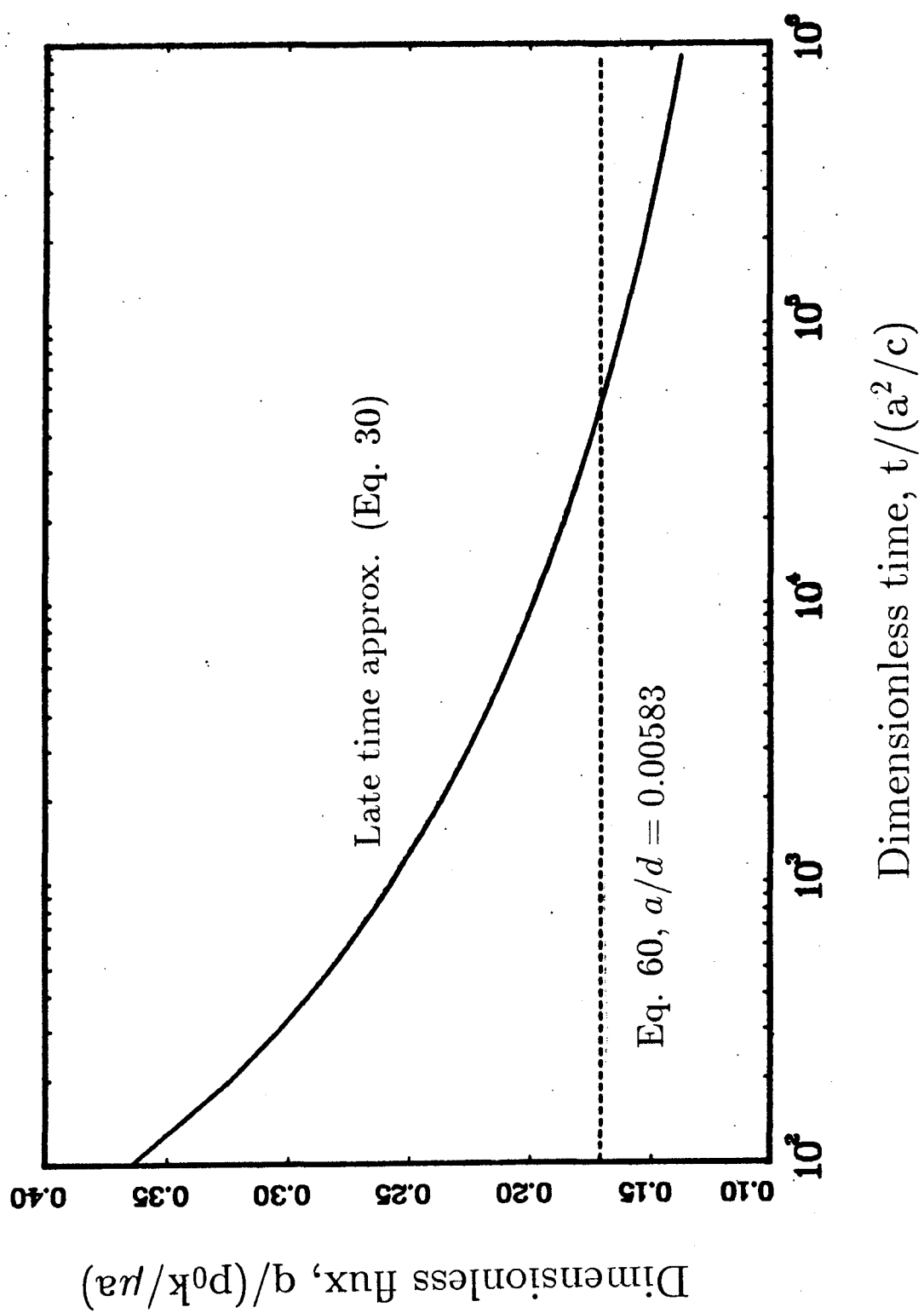


Figure 30: Comparison of transient (Eq. 30) and steady-state (Eq. 60) solutions for flux to a tunnel.

Distribution:
Unlimited Release
UC-70

U. S. Department of Energy, (5)
Office of Civilian Radioactive Waste Management
Office of Geologic Repositories
Forrestal Building
Washington, DC 20585

Associate Director

William J. Purcell — RW-20

Director, Repository Coordination Div.

T. H. Isaacs — RW-22

Director, Engineering & Licensing

Ralph Stein — RW-23

Director, Geosciences & Technology

Ralph Stein, Actg. — RW-24

Director, Siting Division

Ellison Burton — RW-25

U. S. Department of Energy (3)

Albuquerque Operations Office

P.O. Box 5400

Albuquerque, NM 87185

R. G. Romatowski

J. E. Bickel

D. G. Jackson, Director, Public Affairs Division

U. S. Department of Energy (8)

WIPP Project Office (Carlsbad)

P.O. Box 3090

Carlsbad, NM 88221

J. Tillman (4)

A. Hunt

G. Pappas (2)

R. Eastmond

U. S. Department of Energy, SRPO (4)

Salt Repository Project Office

505 King Avenue

Columbus, OH 43201

Jeff O. Neff

R. Wunderlich

G. Appel

R. Wu

U. S. Department of Energy
Research & Technical Support Division
P. O. Box E
Oak Ridge, TN 37830
D. E. Large

U. S. Department of Energy
Richland Operations Office
Nuclear Fuel Cycle & Production Division
P.O. Box 500
Richland, WA 99352
R. E. Gerton

U. S. Department of Energy (3)
Office of Defense Waste and
Transportation Management
Washington, DC 20545
J. E. Dieckhoner — DP-122
L. H. Harmon — DP-121
A. Follett — DP-121

U. S. Department of Energy (2)
Idaho Operations Office
Fuel Processing and Waste
Management Division
785 DOE Place
Idaho Falls, ID 83402

U. S. Department of Energy (4)
Savannah River Operations Office
Waste Management Project Office
P.O. Box A
Aiken, SC 29801
S. Cowan
W. J. Brumley
J. R. Covell
D. Fulmer

U. S. Department of the Interior
959 National Center
Geological Survey
Reston, Virginia 22092
E. Roedder

U. S. Nuclear Regulatory Commission (4)
Division of Waste Management
Mail Stop 623SS
Washington, DC 20555

Michael Bell
Hubart Miller
Jacob Philip
NRC Library

F. R. Cook
Nuclear Regulatory Commission
HLW Licensing Branch, Materials Section
MS 905 SS
Washington, DC 20555

U. S. Geological Survey
Special Projects
MS954, Box 25046
Denver Federal Center
Denver, CO 80255
R. Snyder

U. S. Geological Survey
Conservation Division
Attn: W. Melton
P.O. Box 1857
Roswell, NM 88201

U. S. Geological Survey (2)
Water Resources Division
Western Bank Bldg.
505 Marquette, NW, #720
Albuquerque, NM 87102
H. Lee Case
Peter Davies

State of New Mexico (3)
Environmental Evaluation Group
320 Marcy Street
P.O. Box 968
Santa Fe, NM 87503
Robert H. Neill, Director

NM Department of Energy & Minerals
P.O. Box 2770
Santa Fe, NM 87501
Kasey LaPlante, Librarian

New Mexico Bureau of Mines (2)
and Mineral Resources
Socorro, NM 87801
F. E. Kottolowski, Director
J. Hawley

Battelle Memorial Institute (21)
Project Management Division
505 King Avenue
Columbus, OH 43201
ONWI Library
W. Carbiener, General Manager (3)
S. Basham
D. E. Clark
S. Goldsmith
J. E. Hanley
P. Hoffman
H. R. Hume
H. N. Kalia
J. Kirchner
S. Matthews
D. Moak
J. Moody
T. Naymik
L. Page
G. Raines
J. Schornhorst
O. Swanson
J. Treadwell

Battelle Pacific Northwest Laboratories (6)
Battelle Boulevard
Richland, WA 99352
D. J. Bradley
J. Relyea
R. E. Westerman
S. Bates
H. C. Burkholder
L. Pederson

Bechtel Inc. (6)
P.O. Box 3965
45-11-B34
San Francisco, CA 94119

E. Weber
M. Beathard
H. Taylor
P. Frobenius
D. L. Wu
W. T. Li

INTERA Technologies, Inc. (2)
6850 Austin Center Blvd., #300
Austin, TX 78731
G. E. Grisak
J. F. Pickens

INTERA Technologies, Inc.
P.O. Box 2123
Carlsbad, NM 88221
Wayne Stensrud

IT Corporation (3)
P.O. Box 2078
Carlsbad, NM 88221
W. Patrick
R. McKinney
D. Winstanley

IT Corporation (2)
2340 Alamo, SE
Suite 306
Albuquerque, NM 87106
W. R. Coons
P. Kelsall

RE/SPEC, Inc. (7)
P. O. Box 725
Rapid City, SD 57701
P. F. Gnirk
L. L. Van Sambeek
D. B. Blankenship
T. Brandshang
G. Callahan
T. Pfeifle
J. L. Ratigan

RE/SPEC, Inc.
P.O. Box 14984
Albuquerque NM 87191
S. W. Key

E. I. DuPont de Nemours Company (6)
Savannah River Laboratory
Aiken, SC 29801

N. Bibler
E. L. Albenisius
M. J. Plodinec
G. G. Wicks
C. Juntzen
J. A. Stone

E. I. Dupont de Nemours Company
Savannah River Plant
Aiken, SC 29801
R. Baxter

George Dymmel
SAIC
101 Convention Center Dr.
Las Vegas, NV 89109

Systems, Science, and Software (2)
Box 1620
La Jolla, CA 92038
E. Peterson
P. Lagus

University of Arizona (2)
Department of Nuclear Engineering
Tucson, AZ 85721
J. G. McCray
J. J. K. Daemen

University of California (2)
Department of Nuclear Engineering
Berkeley, CA 94720
T. H. Pigford
D. R. Olander

University of New Mexico (2)
Geology Department
Albuquerque, NM 87131
D. G. Brookins
Library

The Pennsylvania State University (3)
Materials Research Laboratory
University Park, PA 16802

Della Roy
Rustrum Roy
Will White

Texas A&M University
Center of Tectonophysics
College Station, TX 77840
John Handin

University of Texas at El Paso
Department of Geological Sciences
El Paso, TX 79968
D. W. Powers

Westinghouse Electric Corporation (9)
P.O. Box 2078
Carlsbad, NM 88221

P. Mairson
V. DeJong
W. Chiquelin
T. Dillon
V. Likar
J. Johnson
J. Sadler
R. Kehrman
Library

National Academy of Sciences, WIPP Panel:

Konrad B. Krauskopf
Stanford University
Department of Geology
Stanford, CA 94305

Frank L. Parker
Vanderbilt University
Department of Environmental and
Water Resources Engineering
Nashville, TN 37235

John O. Blomeke
Oak Ridge National Laboratory
P.O. Box X
Oak Ridge, TN 37830

National Academy of Sciences, WIPP Panel (continued):

John D. Bredehoeft
Western Region Hydrologist
Water Resources Division
U. S. Geological Survey
345 Middlefield Road
Menlo Park, CA 94025

Dr. Karl P. Cohen
928 N. California Avenue
Palo Alto, CA 94303

Fred M. Ernsberger
1325 N.W. 10th Avenue
Gainesville, FL 32611

Hans P. Eugster
Johns Hopkins University
Department of Earth Sciences
Baltimore, MD 21218

Rodney C. Ewing
University of New Mexico
Department of Geology
Albuquerque, NM 87131

Charles Fairhurst
University of Minnesota
Department of Geological Sciences
Minneapolis, MN 55455

William R. Muehlberger
University of Texas at Austin
Department of Geological Sciences
Austin, TX 78712

D'Arcy A. Shock
233 Virginia
Ponca City, OK 74601

National Academy of Sciences
Committee on Radioactive Waste Management
2101 Constitution Avenue, NW
Washington, DC 20418
Peter Meyers

Hobbs Public Library
509 N. Ship Street
Hobbs, NM 88248
Ms. Marcia Lewis, Librarian

New Mexico Tech
Martin Speere Memorial Library
Campus Street
Socorro, NM 87810

New Mexico State Library
P.O. Box 1629
Santa Fe, NM 87503
Ms. Ingrid Vollenhofer

Zimmerman Library
University of New Mexico
Albuquerque, NM 87131
Zanier Vivian

WIPP Public Reading Room
Atomic Museum
Kirtland East AFB
Albuquerque, NM 87185
Ms. Gwynn Schreiner

WIPP Public Reading Room
Carlsbad Municipal Library
101 S. Halagueno St.
Carlsbad, NM 88220
Lee Hubbard, Head Librarian

Thomas Brannigan Library
106 W. Hadley St.
Las Cruces, NM 88001
Don Dresp, Head Librarian

Roswell Public Library
301 N. Pennsylvania Avenue
Roswell, NM 88201
Ms. Nancy Langston

Svensk Karnbransleforsorjning AB
Project KBS
Karnbranslesakerhet
Box 5864
10248 Stockholm, SWEDEN
Fred Karlsson

Institut für Tieflagerung (4)
Theodor-Heuss-Strasse 4
D-3300 Braunschweig
Federal Republic of Germany

K. Kuhn
N. Jockwer
H. Gies
P. Faber

Bundesanstalt für Geowissenschaften
und Rohstoffe
Postfach 510 153
3000 Hannover 51
Federal Republic of Germany
Michael Langer

Hahn-Mietner-Institut für Kernforschung
Glienicker Strasse 100
100 Berlin 39
Federal Republic of Germany
Werner Lutze
Klaus Eckart Maass

Bundesministerium für Forschung und
Technologie
Postfach 200 706
5300 Bonn 2
Federal Republic of Germany
Rolf-Peter Randl

Physikalisch-Technische Bundesanstalt (2)
Bundesanstalt 100, 3300 Braunschweig
Federal Republic of Germany
Helmut Rothemeyer
Peter Brenneke

Kernforschug Karlsruhe (3)
Postfach 3640
7500 Karlsruhe
Federal Republic of Germany
R. Koster
Reinhard Kraemer
K. D. Closs

Studiecentrum Voor Kernenergie (2)
Centre D'Energie Nucleaire
SCK/CEN
Boeretang 200
B-2400 Mol
Belgium

Mr. A. Bonne
Pierre Van Iseghem

Atomic Energy of Canada, Ltd. (2)
Whiteshell Research Estab.
Pinewa, Manitoba
Canada ROE 1L0
Peter Haywood
John Tait

Dr. D. K. Mukerjee
Ontario Hydro Research Lab
800 Kipling Avenue
Toronto, Ontario, Canada
MBZ 554

Claude Sombret
Centre D'Etudes Nucleaires
De La Vallee Rhone
CEN/VALRHO
S.D.H.A. BP 171
30205 Bagnols-Sur-Ceze
France

Mr. Jean-Pierre Olivier
OECD Nuclear Energy Agency
Division of Radiation Protection
and Waste Management
38, Boulevard Suchet
75016 Paris, FRANCE

D. R. Knowles
British Nuclear Fuels, plc
Risley, Warrington, Cheshire WA3 6AS
1002607 GREAT BRITAIN

Shingo Tashiro
Japan Atomic Energy Research Institute
Tokai-Mura, Ibaraki-Ken
319-11 JAPAN

Netherlands Energy Research Foundation ECN (2)
3 Westerduinweg
P.O. Box 1
1755 ZG Petten
THE NETHERLANDS
Tuen Deboer, Mgr.
L. H. Vons

Titanium Metals Corp. of America
Henderson Technical Laboratory
P.O. Box 2128
Henderson, NV 89015
R. W. Schulz

Woodward-Clyde Consultants
Library Western Region
3 Embarcadero Center, Suite 700
San Francisco, CA 94111
Anne T. Harrigan, Librarian
Charles Taylor

Prof. Pedro Macedo
Catholic University of America
Vitreous State Laboratory
B-2 Kean Hall
Washington, D.C. 20064

Dr. R. O. Pohl
Cornell University
Department of Physics
Clark Hall
Ithaca, NY 14853

University of Florida (2)
Department of Materials Science
and Engineering
Gainesville, FL 32611
David Clark
Larry Hench

Pannell Library
New Mexico Junior College
Lovington Highway
Hobbs, NM 88240
Ms. Ruth Hill

George Pinder
Princeton University
Department of Civil Engineering
Princeton, NJ 08540

Argonne National Laboratory (5)
9700 South Cass Avenue
Argonne, IL 60439

A. M. Friedman
D. Hambeley
W. Harrison
N. Meldgin
M. Steindler

Brookhaven National Laboratory (3)
Associated Universities, Inc.
Upton, NY 11973

Cal Brewster, Bldg. 830
P. Colombo, Dept of Applied Sciences
Paul W. Levy, Senior Scientist

Los Alamos Scientific Laboratory
Los Alamos, NM 87545
B. Erdal, CNC-11

Oak Ridge National Laboratory (4)
Box Y
Oak Ridge, TN 37830
R. E. Blanko
E. Bondietti
C. Claiborne
G. H. Jenks

Oak Ridge National Laboratory, Bldg. 2001
Ecological Sciences Information Center
P.O. Box X
Oak Ridge, TN 37830
C. S. Fore

Rockwell International (2)
Rocky Flats Plant
Golden, CO 80401
W. S. Bennett
C. E. Wickland

Rockwell International (3)
Atomics International Division
Rockwell Hanford Operations
P.O. Box 800
Richland, WA 99352
J. Nelson (HWVP)
P. Salter
W. W. Schultz

Sandia Internal:

1510 J. W. Nunziato
1511 D. K. Gartling
1511 R. R. Eaton
1511 D. F. McTigue
1512 J. C. Cummings
1513 D. W. Larson
1520 C. W. Peterson, Jr.
1521 R. D. Krieg
1530 L. W. Davison
1540 W. C. Luth
1542 W. R. Wawersik
1542 D. H. Zeuch
1543 T. M. Gerlach
1543 J. L. Krumhansl
1543 H. W. Stockman
1550 R. C. Maydew
3141 D. E. Robertson, Actg. (Library) (5)
3151 W. L. Garner, For: Doe/TIC (Unlimited Release) (3)
3154-3 C. H. Dalin, For: DOE/TIC (28)
6000 D. L. Hartley
6300 R. W. Lynch
6310 T. O. Hunter
6330 W. D. Weart
6330 G. R. Romero
6331 A. R. Lappin
6331 R. L. Beauheim
6332 D. J. Borns
6331 S. J. Lambert
6331 K. L. Robinson
6331 C. L. Stein
6331 D. Tomasko
6332 L. D. Tyler
6332 J. G. Arguello
6332 R. Beraun
6332 R. V. Matalucci
6332 M. A. Molecke
6332 D. E. Munson
6332 E. J. Nowak (50)
6332 R. J. Roginski
6332 J. C. Stormont
6332 T. M. Torres

6332 F. G. Yost
6332 Sandia WIPP Central Files (SWCF 510 PS/DE Permanent)
6334 D. R. Anderson
6334 S. G. Bertram
6334 L. H. Brush
6334 L. S. Gomez
6334 J. P. Hickerson, Jr.
6334 R. L. Hunter
6334 M. G. Marietta
6334 A. K. Rutledge
7100 C. D. Broyles
7110 J. D. Plimpton
7116 S. R. Dolce
7116 C. W. Cook
7120 M. J. Navratil
7125 R. L. Rutter
7125 J. T. McIlmoyle
7130 J. D. Kennedy
7133 R. D. Statler
7133 J. W. Mercer
7133 H. C. Walling
7135 P. D. Seward